



#### **OPEN ACCESS**

EDITED BY Jiansen He, Peking University, China

REVIEWED BY Gilbert Pi. Charles University, Czechia Yutian Chi, University of Science and Technology of China China Jianpeng Guo, Beijing Normal University, China

\*CORRESPONDENCE Chenyu Shi, 

RECEIVED 16 August 2025 REVISED 17 October 2025 ACCEPTED 17 October 2025 PUBLISHED 24 November 2025

Zhao X, Shi C, Liu X, Feng X, Zhou Y, Xiang N, Deng L, Kuznetsov A and Möstl C (2025) Mathematical expressions of the drag-based models for predicting the arrival time of coronal mass ejection and their development and evolutionary processes. Front. Astron. Space Sci. 12:1686823. doi: 10.3389/fspas.2025.1686823

#### COPYRIGHT

© 2025 Zhao, Shi, Liu, Feng, Zhou, Xiang, Deng, Kuznetsov and Möstl. This is an open-access article distributed under the terms of the Creative Commons Attribution License (CC BY). The use, distribution or reproduction in other forums is permitted, provided the original author(s) and the copyright owner(s) are credited and that the original publication in this journal is cited, in accordance with accepted academic practice. No use, distribution or reproduction is permitted which does not comply with these terms.

# Mathematical expressions of the drag-based models for predicting the arrival time of coronal mass ejection and their development and evolutionary processes

Xinhua Zhao<sup>1</sup>, Chenyu Shi<sup>1,2,3</sup>\*, Xiao Liu<sup>2</sup>, Xueshang Feng<sup>1,4</sup>, Yufen Zhou<sup>1</sup>, Nanbin Xiang<sup>1,5</sup>, Linhua Deng<sup>6</sup>, Alexey Kuznetsov<sup>7</sup> and Christian Möstl<sup>8</sup>

<sup>1</sup>State Key Laboratory of Solar Activity and Space Weather, National Space Science Center, Chinese Academy of Sciences, Beijing, China, <sup>2</sup>School of Mathematics and Statistics, Henan Normal University, Xinxiang, China, <sup>3</sup>University of Chinese Academy of Sciences, Beijing, China, <sup>4</sup>State Key Laboratory of Solar Activity and Space Weather, School of Aerospace, Harbin Institute of Technology, Shenzhen, China, <sup>5</sup>Yunnan Observatories, Chinese Academy of Sciences, Kunming, China, <sup>6</sup>School of Mathematics and Computer Science, Yunnan Minzu University, Kunming, China, <sup>7</sup>Institute of Solar-Terrestrial Physics, Irkutsk, Russia, <sup>8</sup>Austrian Space Weather Office, GeoSphere Austria, Graz,

As one of the most violent solar activities, coronal mass ejections (CMEs) are eruptions of the large-scale magnetized plasma from the Sun's upper atmosphere into interplanetary space. The Earth-directed CMEs will cause significant disturbances to the solar-terrestrial environment, which in return threaten the safety of the communication, navigation, and ground technology systems. Therefore, predicting whether and when a CME will reach the Earth is an important ingredient of space weather research and forecasting. One commonly used prediction model for the CME's propagation and arrival time is the Drag-Based Model (DBM), which considers the drag force acting on interplanetary CMEs (ICMEs) to explain how CMEs move through the solar wind. In this paper, we outline five routes for the development and evolution of the family models of DBM: 1. The DBM  $\rightarrow$  ELEvoHI (Ellipse Evolution Model Based on HI Observations) series; 2. The DBM → LSF-DBM (Least-Squares Fitting Drag-Based Model) series; 3. The DBM → PDBM (Probabilistic Drag-Based Model) series; 4. The DBM  $\rightarrow$  ExDBM (Extended Drag-Based Model); 5. The DBM  $\rightarrow$ EnDBM (Enhanced Drag-Based Model) Series. We clarify the development and evolution process of the model's mathematical expressions along each route as well as their connections. Finally, we provide a summary of the various models, comparing their similarities and differences, as well as their strengths and weaknesses, and suggest potential improvements.

coronal mass ejection, drag-based model, mathematical expression, arrive time prediction, space weather

# 1 Introduction

Coronal mass ejection (CME) refers to the phenomenon of the large-scale magnetized plasma in the Sun's upper atmosphere being ejected outward into interplanetary space, and is believed to one of the most intense solar activities in the solar atmosphere. When propagating into interplanetary space, it is termed an interplanetary coronal mass ejection (ICME) (Vršnak, 2021). The interplanetary space between Sun and Earth often experiences significant disturbances from CMEs and their associated shocks, which are the primary drivers of hazardous space weather and capable of generating substantial geoeffective consequences (Wang et al., 2013). The Earth-directed CMEs may cause harmful effects on the near-Earth spacecraft, communication and navigation systems, safety of astronauts, and ground-based technology systems (such as power grids and oil pipelines) (Boteler et al., 1998). Therefore, predicting whether and when the CME will reach Earth has become an important aspect of space weather research and forecasting.

In the literature, the arrival time forecast of CMEs and their related shocks can be traced back to at least the early 70s of the last century. After half a century of development, dozens of the forecasting models have been developed. They include the Empirical CME Arrival (ECA) and Empirical Shock Arrival (ESA) model (Gopalswamy et al., 2001), the expansion speed model (Schwenn et al., 2005), the Drag-Based Model (DBM) (Vršnak et al., 2013) and its variants, the "Fearless Forecast" modes [including the Shock Time Of Arrival (STOA), Interplanetary Shock Propagation Model (ISPM), and Hakamada-Akasofu-Fry/version-2 (HAFv.2)] (Fry et al., 2001; Smith and Dryer, 1990), the series of Shock Propagation Model (SPM) models (Feng and Zhao, 2006; Zhao and Feng, 2014), the Cone + HAF model (Wang et al., 2018), the STOAF and STOASF model (Liu and Qin, 2012), the MHD numerical models (including the Wang-Sheeley-Arge (WSA)-ENLIL + Cone (Odstrcil et al., 2004), Heliosphere 3D magnetohydrodynamics (H3DMHD) (Wu et al., 2011), Space Weather Modeling Framework (SWMF) (Toth et al., 2012), CORona-HELiosphere (CORHEL) (Riley et al., 2013), and Solar-InterPlanetary Conservation Element and Solution Element magnetohydrodynamic (SIP-CESE MHD) (Feng et al., 2007; Feng et al., 2012; Feng, 2020)), the machine learning models (Sudar et al., 2016; Liu et al., 2018; Guastavino et al., 2023; Alobaid et al., 2022; Minta et al., 2023; Li et al., 2024), and so on. More information about these models can be found in these review papers (Siscoe and Schwenn, 2006; Zhao and Dryer, 2014; Vourlidas et al., 2019).

Currently, all kinds of prediction models for the CME arrival time have encountered a plateau for improving prediction accuracy, and it is difficult to achieve significant breakthroughs (Kay et al., 2024; Yordanova et al., 2024). Especially, there is still a considerable distance between the prediction accuracy and the actual demand. The low success rate will cause many "false alarms", while the large prediction time error will make people take unnecessary evasive measures for too long. The losses caused by these evasive measures sometimes may exceed the impact of the space weather event itself. Among the predictive models mentioned above, the series of the DBM models is the most commonly used model to predict the CME's arrival time, especially suitable for describing the kinematics of CMEs after their rapid acceleration

phases. Therefore, it is necessary to conduct an in-depth research on the DBM models. It is essential to sort out the evolution processes and correlations of mathematical expressions between its different versions, and discover possible improvement directions to improve the accuracy of the CME arrival time prediction.

During the propagation in the heliosphere, ICMEs are subjected to three principal forces governing their evolution: the Lorentz force, the gravitational force, and the aerodynamic drag induced by the interaction with the background solar wind (Cargill, 2004). Emerging in the Sun's upper atmosphere, CMEs are initially magnetically accelerated by the Lorentz force. As the eruption progresses, this force continues to drive the CME into the solar wind (Vršnak and Gopalswamy, 2002). Observational data indicate that the kinematic behavior of CMEs exhibits a speed dependence on interaction with the solar wind: (1) ICMEs slower than the solar wind exhibit acceleration, (2) whereas faster ICMEs show deceleration (Čalogović et al., 2021; Shanmugaraju and Vršnak, 2014; Vršnak et al., 2013). Based on the observed phenomenon, DBM assumes that in the later stage (typically when the radial distance exceeds 20 solar radii), the ICME is only subject to the drag force (Vršnak and Gopalswamy, 2002; Vršnak et al., 2013; Vakhrusheva et al., 2024), and the critical factors to ICME propagation are both its initial physical parameters and the background solar wind conditions (Vršnak et al., 2013).

As one of the most widely used analytical tools for predicting CME arrivals, DBM describes the propagation of CMEs in the solar wind based on the kinematic equations of the corresponding ICME determined by the drag force, enabling predictions of both transit time and propagation speed at Earth or other specified heliospheric targets (Čalogović et al., 2021; Vršnak et al., 2013; Chierichini et al., 2024). DBM has the characteristics of simplicity and extremely short calculation time, enabling us to obtain reliable estimates of the transit time and propagation speed of the CME at a lower computational cost (Čalogović et al., 2021; Chierichini et al., 2024), and it is thus extremely useful for real time forecasts. Different versions of the DBM have been developed, and they are different from each other in their dependence on the initial geomagnetic parameters of the input CMEs or in the different theoretical propagation processes of the CMEs (Napoletano et al., 2018). These different versions make up a large family of the DBM.

In this work, the development and evolution of the DBM family will be traced along five routes. In the first route, the CME's shape is treated as a self-similar ellipse, and the distance and speed equations are derived for any point of the CME front. Then, a deformed CME front as well as a varying background solar wind speed is introduced for improvements. In the second route, the CME geometry is treated as either a self-similar cone or a flattening cone. Subsequently, a flattening conical geometry equation is proposed. In the third route, the values of the drag parameter and the background solar wind speed are obtained by inversely solving the analytical solutions of the DBM. In the fourth route, an acceleration term describing the other forces besides the drag force is used to improve the model. In the fifth route, a GCS model and a prolate spheroid bubble model are adopted to depict the CME geometry and the shock geometry, respectively.

Through the systematic analysis of the mathematical expressions and their development and evolution in the DBMs for the CME arrival time prediction, the evolutionary processes and correlations of the mathematical expressions between different versions of the DBM for the CME arrival time prediction can be sorted out. This enables the revelation of the underlying evolution patterns of the DBM and the identification of potential improvement directions for it. Such insights will facilitate further advancements in the DBM, thereby enhancing the predictive accuracy of the model regarding CME arrival time and mitigating the adverse effects of the CME. The remainder of this paper is structured as follows. Section 2 introduces the basic version of DBM. Section 3 presents the evolutionary process of the DBM models along these five routes. As a useful supplement, Section 4 lists some other DBM models without a clear development path. Conclusions and discussions are provided in Section 5.

### 2 The basic version of DBM

The fundamental form of the DBM was initially introduced by Vršnak and Žic (2007) and subsequently refined and adjusted by Vršnak et al. (2013). Through analytical approaches, explicit solutions were obtained for two key CME parameters by Vršnak et al. (2013). Their study successfully solved the CME motion equations, determining both transit time and propagation speed. These analytical solutions not only provide immediate practical predictions but also substantially improve the operational effectiveness of the DBM, facilitating its broader applications in space weather forecasting. The basic version of DBM is the simplest version of the DBM family, which does not consider the geometry of the CME, but only considers the propagation of the CME apex, and is a one-dimensional model (Dumbović et al., 2021).

## 2.1 DBM in 2007

In order to study the dependence of ICME transit times on the initial CME speed ("take-off" speed) and solar wind speed, Vršnak and Žic (2007) compared the observed ICME transit times with the CME take-off speed and the solar wind speed, confirmed the existence of the correlation between them, and proposed the basic form of the DBM.

The model assumes that ICME maintains constant mass throughout propagation (M = const), the ICME's cross-sectional area is proportional to the square of the heliocentric distance ( $A \propto R^2$ ), and the ICME is influenced exclusively by the drag force during the later stage of propagation. Additionally, the model assumes that when the distance of ICME from the Sun is greater than 20 solar radii, the solar wind speed remains unchanged ( $w \approx \text{const}$ ), while its density exhibits an inverse relationship with heliocentric distance ( $\rho_w \approx R^{-2}$ ). The dimensionless drag coefficient generally remains unchanged with the distance ( $C_d \approx \text{const}$ ), then the drag parameter is constant:  $y = \frac{C_d A \rho_w}{M} = \text{const}$ . Subsequently, based on a = -y(v-w)|v-w|, the numerical calculation of the propagation time (TT) of ICME from 20 solar radii to Earth under different solar wind speeds is obtained as a function of the CME's initial speed at

20 solar radii ( $v_0$ ), where a is the acceleration of ICME and v is the speed of CME.

#### 2.2 DBM in 2013

Vršnak et al. (2013) improved the above DBM and proposed explicit solutions of the transit time and propagation speed of ICME at Earth, which provides a direct application for the CME arrival prediction. Unlike the DBM in 2007, the DBM in 2013 considered the virtual mass of the ICME was  $M_{\rm v} \approx \frac{\rho_{\rm w} V}{2}$ . In this case,  $\gamma = \frac{C_{\rm d} A \rho_{\rm w}}{M + M_{\rm v}} = \frac{C_{\rm d} A}{V(\rho + \frac{\rho_{\rm w}}{2})} = \frac{C_{\rm d} A}{A L \left(\frac{\rho}{\rho_{\rm w}} + \frac{1}{2}\right)} = \frac{C_{\rm d}}{L \left(\frac{\rho}{\rho_{\rm w}} + \frac{1}{2}\right)}$ , where V is the volume of ICME, A is the cross-sectional area of ICME, A is the thickness of ICME in the radial direction,  $V \approx A L$ ,  $\rho$  is the density of ICME. From the expression of  $\gamma$ , we see that when  $\rho \gg \rho_{\rm w}$ , only the ICME mass needs to be considered.

The model applies only when the ICME is at least 20 solar radii away from the Sun. Under this condition,  $A \propto R^2$ , M = const,  $C_{\rm d} = \text{const}$ , and w = const, consistent with the DBM proposed in 2007. In addition, the model assumes  $\rho \gg \rho_{\rm w}$ , from which we derive  $\gamma = \text{const}$ 

Considering that the CME is influenced exclusively by the drag force during the later stage of CME propagation, based on the assumption (w = const; y = const), the explicit solutions of the transit time and propagation speed of ICME at Earth can be obtained by solving a = -y(v - w)|v - w| analytically.

The mathematical derivation processes for solving the explicit solutions of the transit time and propagation speed of ICME at Earth's orbit are as follows:

$$a = -\gamma(\nu - w)|\nu - w| \tag{1}$$

Equation 1 can be transformed into  $\frac{dv(t)}{dt} = \pm \gamma(v(t) - w)^2$ . Let y(t) = v(t) - w, then  $\frac{dy(t)}{dt} = \pm \gamma y^2(t)$ . Thus  $\frac{dy(t)}{y^2(t)} = \pm \gamma dt$ ,  $y^{-1}(t) = \pm \gamma t + C_1$ , and  $y(t) = \frac{1}{C_1 \pm \gamma t}$ . So  $v(t) = \frac{1}{C_1 \pm \gamma t} + w$ . When t = 0,  $v(t) = v_0$ . Then  $v_0 = \frac{1}{C_1} + w$ , thus  $C_1 = \frac{1}{v_0 - w}$ , and we get

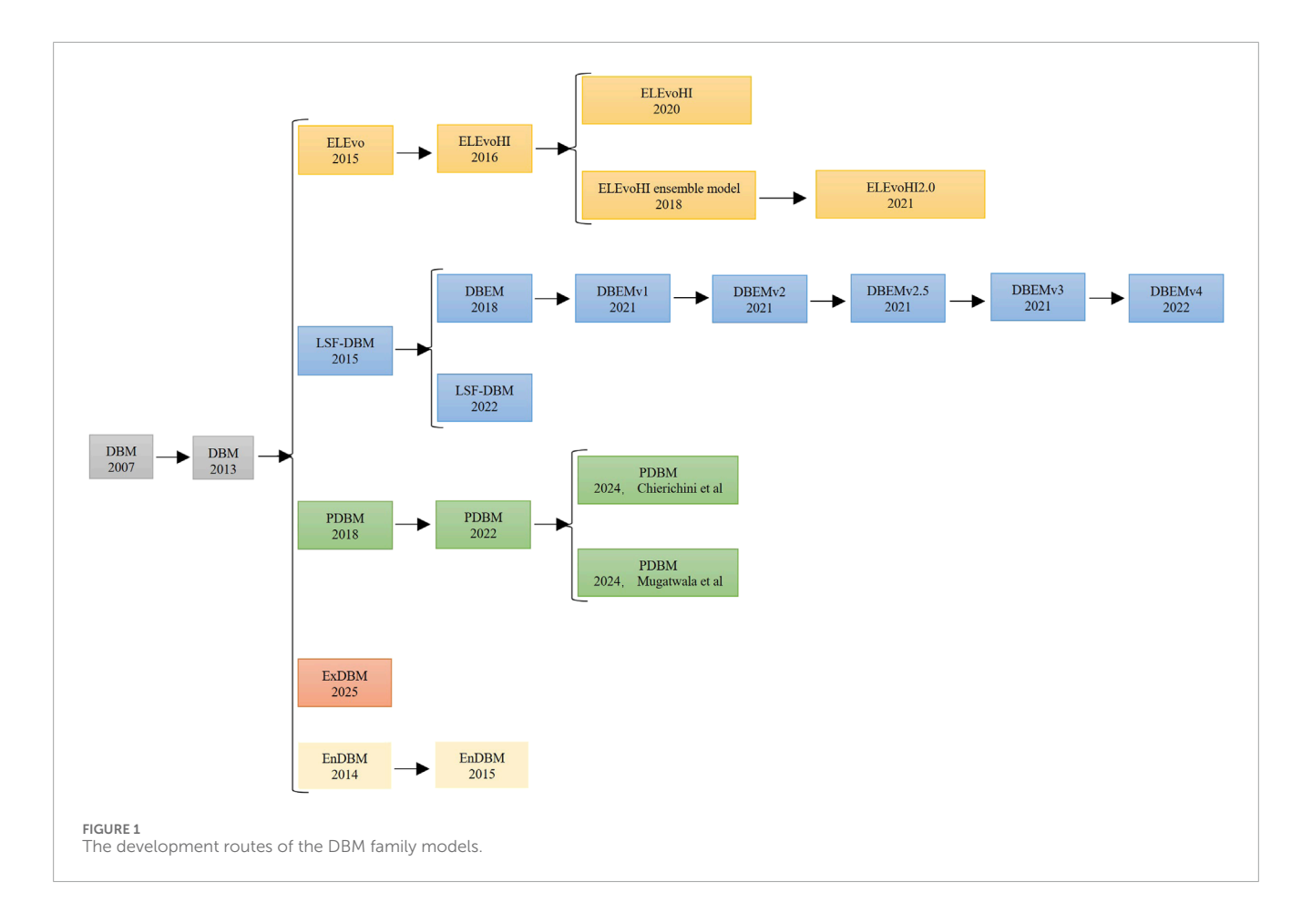
$$\nu(t) = \frac{1}{\frac{1}{\nu_0 - w} \pm \gamma t} + w = \frac{\nu_0 - w}{1 \pm \gamma (\nu_0 - w)t} + w \tag{2}$$

Equation 2 can be transformed into  $\frac{dR(t)}{dt} = \frac{v_0 - w}{1 \pm y (v_0 - w)t} + w.$  Integrate both sides of the equation and we get  $R(t) = \int \frac{1}{1 \pm y (v_0 - w)t} dt + wt + C_2 = \pm \frac{1}{y} \ln \left[ 1 \pm y (v_0 - w)t \right] + wt + C_2$ . When t = 0,  $R(t) = R_0$ . Thus  $C_2 = R_0$ , and we get

$$R(t) = \pm \frac{1}{\gamma} \ln \left[ 1 \pm \gamma (\nu_0 - w)t \right] + wt + R_0$$
 (3)

Equations 2, 3 are the explicit solutions for the ICME's propagation speed and transit time upon arrival. When  $\nu_0 > w$ , the sign takes "+", indicating the ICME is undergoing deceleration. When  $\nu_0 < w$ , it takes "–", indicating the ICME is undergoing acceleration.

The input parameters of DBM are: the initial time  $(t_0)$ , the initial speed of the ICME  $(v_0)$ , the initial radial distance of the ICME  $(R_0)$ , the speed of the background solar wind (w), and the drag parameter (y). The output parameters of the DBM are: Sun-Earth transit time (TT) and the propagation speed of ICME at 1AU  $(v_{1AU})$ .



# 3 The evolution routes based on the basic version of DBM

Up till now, a series of models have been developed based on the basic version of DBM. In this paper, we will sort out the development and evolution of the DBM family along five routes (see Figure 1 for details):

- 1. DBM  $\rightarrow$  Ellipse Evolution Model Based on HI observations (ELEvoHI) model series;
- 2. DBM → Least-Squares Fitting Drag-Based Model (LSF-DBM) series;
- 3. DBM → Probabilistic DBM (PDBM) series;
- 4. DBM → Extend Drag-Based Model (ExDBM);
- 5. DBM → Enhanced Drag-Based Model (EnDBM) series.

In the following, we will introduce the development and evolution of the models along different routes, investigate the relationship between their mathematical expressions of the DBM within each route, and propose the directions of improvement for some routes.

#### 3.1 ELEvoHI model series

Möstl et al. (2015) improved DBM and proposed the ELEvo model. Rollett et al. (2016) improved ELEvo and established the ELEvoHI model. Subsequently, Braga et al.

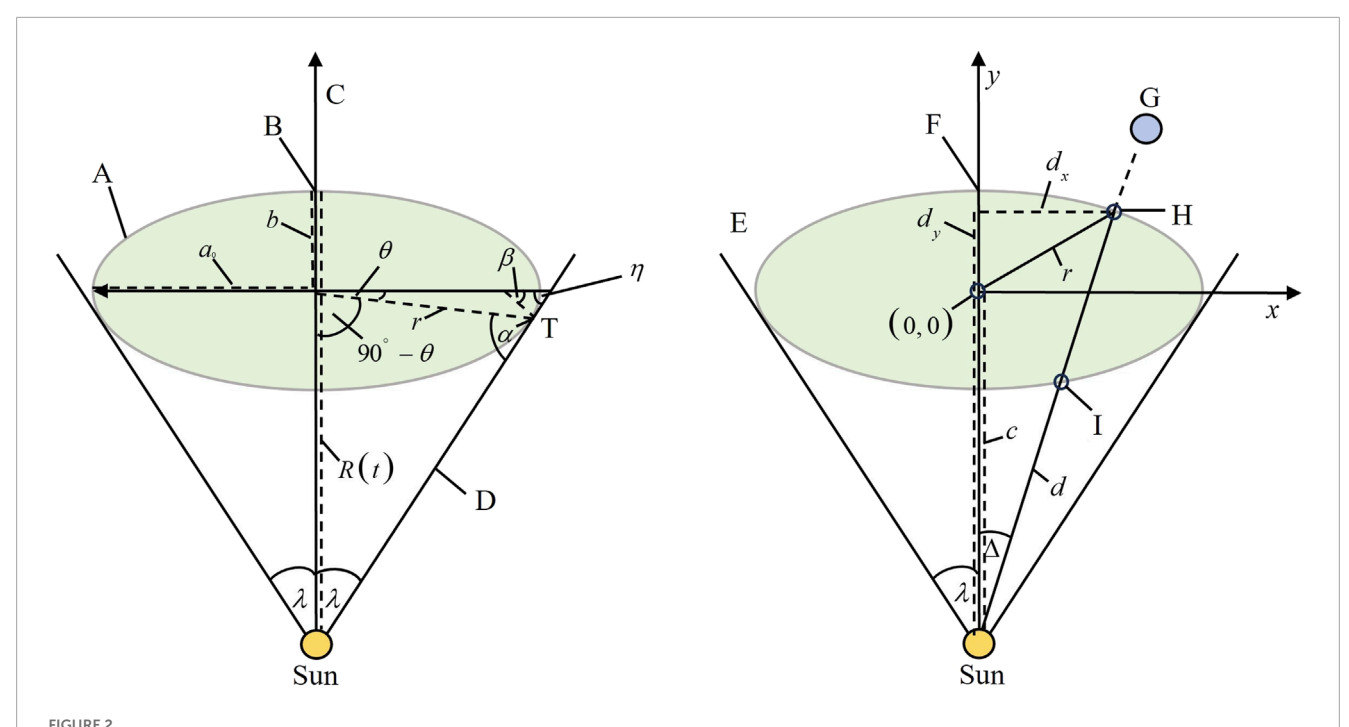
(2020) determined the movement of CME by using the ELEvoHI model within the Heliospheric Imager-1 (HI-1) field of view and using the DBM model outside the HI-1 field of view.

Amerstorfer et al. (2018) refined the ELEvoHI model originally proposed by Rollett et al. (2016), developing it into an ensemble model. Hinterreiter et al. (2021) improved the ELEvoHI ensemble model and proposed the ELEvoHI 2.0 model.

#### 3.1.1 ELEvo model

The ELEvo model (Möstl et al., 2015) assumes that the shape of the CME-driven shock in the ecliptic plane is a self similar expanding ellipse, as shown in Figure 2. Here  $a_0$  refers to a and  $\xi$  refers to  $\omega$  in Figure 5 of Möstl et al. (2015). It also assumes that the half angular width ( $\lambda$ ), the inverse aspect ratio (f), and the propagation direction of the ellipse are constant. Additionally, it assumes that one of the main axes of the ellipse is along the propagation direction throughout the evolution. This model extends the DBM from one dimension to two dimensions. The motion of the ellipse apex is given by the analytical solutions of the DBM. Taking into account the propagation direction of CMEs, this model can predict the arrival time and the propagation speed at time of arrival at any point along the CME front at a specific location in space.

The semi-major axis  $(a_0)$ , the semi-minor axis (b), and the distance from the center of the Sun to the center of the ellipse (c)



(Left) The shape of CME. (Right) The speed along the ellipse front. Originally published in Möstl et al. (2015) with redrawing. A: CME boundary; B: Apex; C: CME central direction; D: Tangent; E: Flank; F: Apex; G: Earth; H: Front solution (+); I: Rear solution (-).

can be transformed into functions of R(t), f, and  $\lambda$  (Equations 4, 5), combined with Figure 2:

$$b = \frac{R(t)\xi \sin \lambda}{\cos(\lambda - \theta) + \xi \sin \lambda}$$
 (4)

$$a_0 = \frac{b}{f}, c = R(t) - b \tag{5}$$

where  $\xi = \sqrt{(f^2 - 1)\cos^2\theta + 1}$ ,  $\theta = \arctan(f^2\tan\lambda)$ . R(t) can be derived from the analytical solutions in the DBM:  $R(t) = \pm \frac{1}{\gamma} \ln\left[1 \pm \gamma(\nu_0 - w)t\right] + wt + R_0$ .

Then the speed along the ellipse front can be calculated as a function of the ellipse parameters, combined with Figure 2:

$$d_{1,2} = \frac{c \cos \Delta \pm \sqrt{(b^2 - c^2) f^2 \sin^2 \Delta + b^2 \cos^2 \Delta}}{f^2 \sin^2 \Delta + \cos^2 \Delta}$$
 (6)

 $v_{\Delta}(t) = \frac{d_1(t)}{R(t)} v(t)$ , where  $\Delta$  is the angle between the CME propagation direction and Earth (or any other planet or spacecraft in the solar wind), and it is a known parameter. v(t) is from the analytical solutions in the DBM. In Equation 6, "+" is taken for the "front" solution  $(d_1)$ , and "–" is taken for the "rear" solution  $(d_2)$ . The CME's propagation speed at arrival time, is determined under two conditions: either the distance equals the target's heliocentric distance, or the arrival time at that location is explicitly defined. Complete expressions for the parameters are available in the cited references (Möstl et al., 2015).

# 3.1.2 ELEvoHI model

Rollett et al. (2016) improved the ELEvo model (Möstl et al., 2015) by replacing coronagraph observations with HI data and

integrating the Fixed- $\phi$  Fitting (FPF) method, the Elliptical Conversion (ElCon) method, the DBM fitting method, and the ELEvo model to develop the ELEvoHI model. The geometry of the CME ellipse adopted in ELEvoHI is shown in Figure 3.

The specific processes of the ELEvoHI model are as follows. Firstly, the time-elongation profile  $(\varepsilon(t))$  is extracted from the HI observations. Then, the FPF method is applied to obtain the propagation direction of the CME ( $\phi$ ). Assuming the values of  $\lambda$ and f of CME as the input parameters of the ElCon method, the distance (R(t)) from the apex of the CME to the center of the Sun is obtained by the ElCon method, and the corresponding speed (v(t)) is subsequently derived by taking the time derivative of this distance. The distance expression from the DBM is employed to fit R(t), yielding values for parameters w, y,  $t_0$ ,  $R_0$ , and  $v_0$ . Finally, these parameters, combined with  $\phi$ ,  $\lambda$  and f are input to the ELEvo model to give both the transit time of CME and its propagation speed upon arrival. The mathematical expressions in the ELEvoHI model are identical to that in the ELEvo model. With reference to Figure 3, the mathematical expressions for converting  $\varepsilon(t)$  to R(t) via the ElCon method are presented as follows (Equations 7–9):

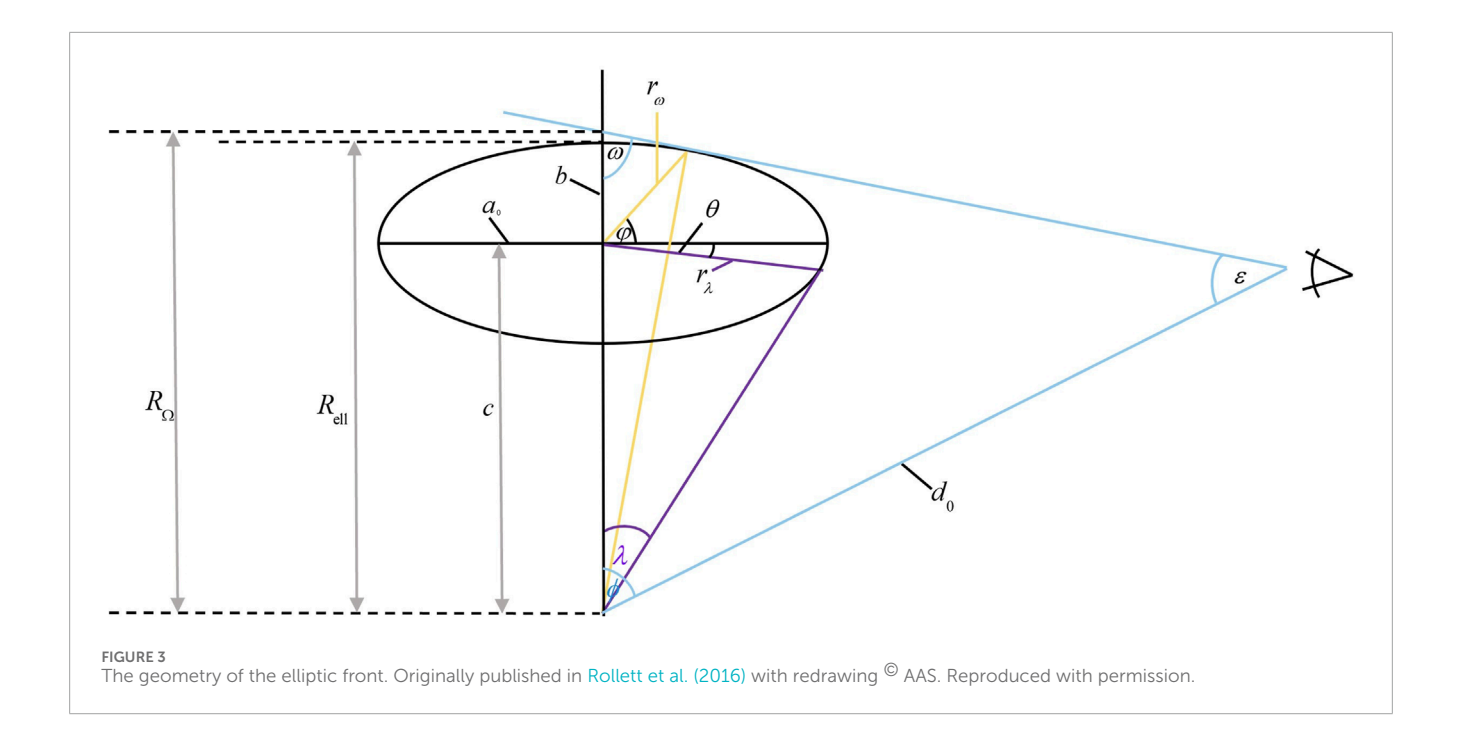
$$b = \frac{d_0 \sin(\varepsilon) \sin(\lambda) \Omega_{\theta} \Omega_{\varphi}}{\sin(90 + \theta - \lambda) \sin(\omega) \Omega_{\varphi} + \sin(90 + \varphi - \omega) \sin(\lambda) \Omega_{\theta}}$$
(7)

$$c = \frac{d_0 \sin(\varepsilon) - r_\omega \sin(90 + \varphi - \omega)}{\sin(\omega)} \text{ or } = \frac{r_\lambda \sin(90 + \theta - \lambda)}{\sin(\lambda)}$$
(8)

Therefore,

$$R(t) = c + b \tag{9}$$

After differentiating R(t) with respect to t, we obtain v(t), where  $\theta = \arctan(f^2 \tan \lambda)$ ,  $\varphi = \arctan(f^2 \tan \omega)$ ,  $\Omega_x = \sqrt{f^2 \cos^2 x + \sin^2 x}$ ,



 $x \in \{\theta, \varphi\}$  and  $\omega = 180^{\circ} - \varepsilon - \phi$ . When  $\varepsilon + \phi < 90^{\circ}$ ,  $\omega = \varepsilon + \phi$ . Besides,  $r_{\omega} = \frac{b}{\sqrt{f^2 \cos^2 \phi + \sin^2 \phi}}$ ,  $r_{\lambda} = \frac{b}{\sqrt{f^2 \cos^2 \theta + \sin^2 \theta}}$ . Complete derivations for the remaining formulas are available in Rollett et al. (2016).

Braga et al. (2020) obtained CME parameters within the HI-1 field of view through the above-mentioned ELEvoHI model by using simultaneous observation data from two perspectives of the HI-1 on STEREO (Solar TErrestrial Relations Observatory)-A and STEREO-B. Outside the HI-1 field of view, assuming that the CME is solely affected by the drag force, the DBM is used to determine the motion of the CME. The mathematical expressions of the DBM used in this model are:

$$\begin{split} F_{\rm drag}[s] &= -M\gamma[s](v[s]-w[s])|v[s]-w[s]| \\ \gamma[s] &= C_{\rm d}[s]n_{\rm SW}[s]\frac{m_{P}A[s]}{M} \\ C_{\rm d}[s] &= 0.148-4.3\times 10^{4}(Re[s])^{-1} + 9.8\times 10^{-9}Re[s] \\ A[s] &= \pi\times R_{\rm CME}^{2}[s]\times \frac{\lambda}{180} \\ w^{2}[s] &= w_{@1{\rm au}}^{2}\Big[1-e^{-(s-r_{1})/r_{a}}\Big] \\ n_{\rm SW}[s] &= \Big(\frac{n_{\rm SW@1au}}{7.2}\Big) \big(3.3\times 10^{5}s^{-2} + 4.1\times 10^{6}s^{-4} + 8\times 10^{7}s^{-6}\big) \end{split}$$

where s is the distance from the Sun along the Sun-Earth line, M is the mass of the CME, v is the speed of the CME, w is the speed of the background solar wind,  $n_{\rm SW}$  is the solar wind proton density,  $m_P$  is the proton mass, A is the cross-sectional area of the CME, Re is the Reynolds number,  $R_{\rm CME}$  is the radius of the CME,  $\lambda$  is the CME half angular width,  $r_1 = 1.5R_{\Theta}$  is the heliocentric distance when the background solar wind speed is 0, and  $r_a = 50R_{\Theta}$  is the heliocentric distance when the background solar wind speed reaches

the asymptotic constant value. More information about the model can be found in the references.

#### 3.1.3 ELEvoHI ensemble model

Amerstorfer et al. (2018) improved the ELEvoHI model proposed by Rollett et al. (2016), and put forward the ELEvoHI ensemble model. When given real-time (near real-time) HI data, this model uses the GCS model to obtain the information of the shape of the CME in the ecliptic plane, and uses the ELEvoHI model to predict the arrival of the CME in real time. It uses different input parameters for the same event by changing the values of  $\phi$ ,  $\lambda$ , and f, and obtains the minimum errors and associated uncertainties of CME arrival time and propagation speed through the ensemble method. Furthermore, this model also constrains the range of the ELEvoHI model's prediction results based on the frequency distribution of the drag parameter, the speed of the background solar wind, initial speed, and initial distance, thereby optimizing the prediction results.

#### 3.1.4 ELEvoHI 2.0 model

Hinterreiter et al. (2021) improved the ELEvoHI ensemble model and proposed the ELEvoHI 2.0 model. The model replaces the elliptical front with a deformed CME front outside the DBM fitting range. Then, during the propagation of CME, its front is continuously affected by the background solar wind conditions, and this effect leads to corresponding morphological adjustments in the CME front. The model also uses the Heliospheric Upwind eXtrapolation model (HUX), the Heliospheric Upwind eXtrapolation with time dependence model (HUXt), and the EUropean Heliospheric FORecasting Information Asset model (EUHFORIA) to consider the varying drag parameters and the background solar wind speed, and uses the analytical solutions of DBM to obtain the arrival time and propagation speed of the CME at any position in the heliosphere. The values of w, and

 $\gamma$  at each time and position in the heliosphere are calculated as follows:

From the aforementioned three solar wind models (HUX, HUXt, and EUHFORIA), we can obtain the parameter w. The expression for drag parameter is  $\gamma = c_{\rm d} \frac{A(r)\rho_{\rm w}}{M}$ , where  $c_{\rm d}=1$ , the background solar wind density  $(\rho_{\rm w})$  can be either derived from the EUHFORIA model or estimated from the HUX and HUXt models using empirical relationships,  $A = \pi r^2 \tan{(\lambda)} \tan{(\kappa/2)}$ , r is the radial distance,  $\lambda$  and  $\kappa$  are assumed to be constant and can be obtained from observations. Furthermore, the model assumes that the CME maintains a constant mass (M) throughout the heliospheric propagation. At the transition point from the fixed front to the deformed front, the DBM fitting method is used to obtain the fitting values of w and y, which can then be used to calculate M, thereby to estimate the value of  $\gamma(r)$  at any position in the heliosphere.

# 3.1.5 The relationship between the mathematical expressions in various models

In contrast to DBM, the ELEvo model assumes that the shape of the CME is elliptic (Möstl et al., 2015), and considers the propagation direction of the CME. In this way the motion of each point along the CME front can be obtained. Therefore, the one-dimensional model is extended to a two-dimensional model after taking into account the evolution of the CME boundary in the ecliptic plane. In ELEvo, the mathematical equations that describes the propagation of the CME apex are the explicit solutions adopted in the DBM.

Compared with the ELEvo model, the ELEvoHI model developed in 2016 uses the HI observation data (Rollett et al., 2016), which has a wider field of view than coronagraphs and can obtain the CME kinematic parameters in a larger heliospheric space. The methods for deriving the expressions of  $\theta$ ,  $r_{\lambda}$ ,  $\varphi$  and  $r_{\omega}$  in the ElCon method are consistent with those in the ELEvo model. Furthermore, the ELEvoHI model uses the ELEvo model to calculate the evolution of the CME boundary in the ecliptic plane.

The ELEvoHI model in 2020, compared with its 2016 version, uses the ELEvoHI model of 2016 within the HI-1 field of view and uses the DBM to describe the propagation of the CME outside the HI-1 field of view. The processes of the ELEvoHI ensemble model in 2018 are consistent with that of the ELEvoHI model in 2016.

Compared with the ELEvoHI ensemble model in 2018, the ELEvoHI 2.0 model in 2021 replaces the elliptical front with a deformed CME front outside the DBM fitting range. It also considers the varying drag parameter and background solar wind speed, and uses the analytical solutions of DBM to obtain the arrival time and propagation speed of the CME. For improvement direction in the future, the following aspects can be considered: (1) The aspect ratio in the ELEvo model could be developed as a function of time (Möstl et al., 2015); (2) More realistic solar wind conditions could be adopted instead of empirical expressions; (3) The mass of CME could be treated as a variable along time or distance.

#### 3.2 LSF-DBM series

In the implementations of the above-mentioned DBM models, their input parameters were typically determined through empirical selection based on the studied events, which are not necessarily suitable for the event being forecasted (Žic et al., 2015). To address this limitation, Žic et al. (2015) developed an optimized approach termed the LSF-DBM in 2015, which determines the optimal input parameters by minimizing the discrepancy between the model predictions and the observations. Sudar et al. (2022) conducted a further study on the shape of the flattening CME front in the LSF-DBM, analyzing the behavior of the CME front, the influence of the drag force on the CME front, the change in the shape of the CME front, and the change in the speed of the CME front over time.

Combining the shape of the flattening CME front in LSF-DBM, Dumbović et al. (2018) proposed DBEM to address the problem of insufficient reliable input data for the CME prediction. Subsequently, the DBEM was developed in 2021 and 2022 to yield the DBEMv3 (Čalogović et al., 2021) and DBEMv4, respectively.

#### 3.2.1 LSF-DBM

LSF-DBM (Žic et al., 2015) assumes that the CME shape is conical, as shown in Figure 3 of Žic et al. (2015). The model dynamically updates the DBM inputs based on the changing of the CME's kinematics as well as the ambient conditions, with parameters optimized via the least-square fitting. The mathematical expressions used in this model are consistent with those in the DBM models mentioned earlier, except that it takes into account the disturbances that the CME experiences during its motion, where the values of the background solar wind speed (w) and the drag parameter (y) vary with time. Since the DBEM developed later (Čalogović et al., 2021; Dumbović et al., 2018) only uses the geometry of the CME assumed in the LSF-DBM, the mathematical expressions of the CME geometry and their mathematical derivation processes (Dumbović et al., 2021) will be introduced in the following content (Equations 10-15). The calculation equations for the initial state of the ICME front are as follows, here r' is r, and  $\psi$  is  $\varphi$  in Figure 3 of Žic et al. (2015):

As shown in Figure 3 of Žic et al. (2015),  $r' = h \tan \lambda$ , then  $R_0 = h + r' = h + h \tan \lambda = h(1 + \tan \lambda)$ . Therefore,  $h = \frac{R_0}{1 + \tan \lambda}$ . Thus

$$R_{\psi} = h \left( \cos \psi + \sqrt{\tan^2 \lambda - \sin^2 \psi} \right) = R_0 \frac{\cos \psi + \sqrt{\tan^2 \lambda - \sin^2 \psi}}{1 + \tan \lambda}$$
(10)

By differentiating both sides of the equation with respect to t, we obtain

$$v_{\psi} = v_0 \frac{\cos \psi + \sqrt{\tan^2 \lambda - \sin^2 \psi}}{1 + \tan \lambda} \tag{11}$$

where the expressions of  $R_0$  and  $\nu_0$  are obtained analytically in the DBM.

#### 1. DBM with a self-similar cone:

At time t, the calculation equations for the initial state of the ICME front are as follows:

$$R(\psi, t) = R(t) \frac{\cos \psi + \sqrt{\tan^2 \lambda - \sin^2 \psi}}{1 + \tan \lambda}$$
 (12)

$$v(\psi,t) = v(t) \frac{\cos \psi + \sqrt{\tan^2 \lambda - \sin^2 \psi}}{1 + \tan \lambda}$$
 (13)

where  $R(t) = \pm \frac{1}{\gamma} \ln \left[ 1 \pm \gamma (v_0 - w)t \right] + wt + R_0$ ,  $v(t) = \frac{v_0 - w}{1 \pm \gamma (v_0 - w)t} + wt$ When  $v_0 > w$ , the sign takes "+"; when  $v_0 < w$ , it takes "-".

#### 2. DBM with a flattening cone:

At time t, the calculation equations for the initial state of the ICME front are as follows:

$$R(\psi, t) = \pm \frac{1}{\nu} \ln \left[ 1 \pm \gamma \left( \nu_{\psi} - w \right) t \right] + wt + R_{\psi}$$
 (14)

$$v(\psi, t) = \frac{v_{\psi} - w}{1 \pm y(v_{\psi} - w)t} + w \tag{15}$$

where  $R_{\psi} = R_0 \frac{\cos \psi + \sqrt{\tan^2 \lambda - \sin^2 \psi}}{1 + \tan \lambda}$ ,  $v_{\psi} = v_0 \frac{\cos \psi + \sqrt{\tan^2 \lambda - \sin^2 \psi}}{1 + \tan \lambda}$ . When  $v_0 > w$ , the sign takes "+"; when  $v_0 < w$ , it takes "-".

Sudar et al. (2022) further developed the equations for the above-mentioned flattening front, where each point of the CME front propagates independently. Based on the equations in DBM, they investigated the morphological evolution characteristics of the CME front as well as the speed variations at any point of the CME front along radial distance, and derived several significant conclusions (Equations 16, 17). The specific processes are as follows:

$$\begin{split} R_0 \frac{\cos \psi + \sqrt{\tan^2 \lambda - \sin^2 \psi}}{1 + \tan \lambda} &= R_0 F(\psi), & v_\psi &= v_0 F(\psi), & R(\psi, t) &= \pm \frac{1}{\gamma} \ln \left[ 1 \pm y \left( v_0 F(\psi) - w \right) t \right] + w t + R_0 F(\psi), & v(\psi, t) &= \frac{v_0 F(\psi) - w}{1 \pm y \left( v_0 F(\psi) - w \right) t} + \frac{1}{\gamma} \left[ \frac{1 + \sin^2 \psi}{1 + \sin^2 \psi} \right] + \frac{1}{\gamma} \left[ \frac{1 + \cos^2 \psi}{1 + \cos^2 \psi} \right] + \frac{1}{\gamma} \left[ \frac{1 + \cos^2 \psi}{1 + \cos^2 \psi} \right] + \frac{1}{\gamma} \left[ \frac{1 + \cos^2 \psi}{1 + \cos^2 \psi} \right] + \frac{1}{\gamma} \left[ \frac{1 + \cos^2 \psi}{1 + \cos^2 \psi} \right] + \frac{1}{\gamma} \left[ \frac{1 + \cos^2 \psi}{1 + \cos^2 \psi} \right] + \frac{1}{\gamma} \left[ \frac{1 + \cos^2 \psi}{1 + \cos^2 \psi} \right] + \frac{1}{\gamma} \left[ \frac{1 + \cos^2 \psi}{1 + \cos^2 \psi} \right] + \frac{1}{\gamma} \left[ \frac{1 + \cos^2 \psi}{1 + \cos^2 \psi} \right] + \frac{1}{\gamma} \left[ \frac{1 + \cos^2 \psi}{1 + \cos^2 \psi} \right] + \frac{1}{\gamma} \left[ \frac{1 + \cos^2 \psi}{1 + \cos^2 \psi} \right] + \frac{1}{\gamma} \left[ \frac{1 + \cos^2 \psi}{1 + \cos^2 \psi} \right] + \frac{1}{\gamma} \left[ \frac{1 + \cos^2 \psi}{1 + \cos^2 \psi} \right] + \frac{1}{\gamma} \left[ \frac{1 + \cos^2 \psi}{1 + \cos^2 \psi} \right] + \frac{1}{\gamma} \left[ \frac{1 + \cos^2 \psi}{1 + \cos^2 \psi} \right] + \frac{1}{\gamma} \left[ \frac{1 + \cos^2 \psi}{1 + \cos^2 \psi} \right] + \frac{1}{\gamma} \left[ \frac{1 + \cos^2 \psi}{1 + \cos^2 \psi} \right] + \frac{1}{\gamma} \left[ \frac{1 + \cos^2 \psi}{1 + \cos^2 \psi} \right] + \frac{1}{\gamma} \left[ \frac{1 + \cos^2 \psi}{1 + \cos^2 \psi} \right] + \frac{1}{\gamma} \left[ \frac{1 + \cos^2 \psi}{1 + \cos^2 \psi} \right] + \frac{1}{\gamma} \left[ \frac{1 + \cos^2 \psi}{1 + \cos^2 \psi} \right] + \frac{1}{\gamma} \left[ \frac{1 + \cos^2 \psi}{1 + \cos^2 \psi} \right] + \frac{1}{\gamma} \left[ \frac{1 + \cos^2 \psi}{1 + \cos^2 \psi} \right] + \frac{1}{\gamma} \left[ \frac{1 + \cos^2 \psi}{1 + \cos^2 \psi} \right] + \frac{1}{\gamma} \left[ \frac{1 + \cos^2 \psi}{1 + \cos^2 \psi} \right] + \frac{1}{\gamma} \left[ \frac{1 + \cos^2 \psi}{1 + \cos^2 \psi} \right] + \frac{1}{\gamma} \left[ \frac{1 + \cos^2 \psi}{1 + \cos^2 \psi} \right] + \frac{1}{\gamma} \left[ \frac{1 + \cos^2 \psi}{1 + \cos^2 \psi} \right] + \frac{1}{\gamma} \left[ \frac{1 + \cos^2 \psi}{1 + \cos^2 \psi} \right] + \frac{1}{\gamma} \left[ \frac{1 + \cos^2 \psi}{1 + \cos^2 \psi} \right] + \frac{1}{\gamma} \left[ \frac{1 + \cos^2 \psi}{1 + \cos^2 \psi} \right] + \frac{1}{\gamma} \left[ \frac{1 + \cos^2 \psi}{1 + \cos^2 \psi} \right] + \frac{1}{\gamma} \left[ \frac{1 + \cos^2 \psi}{1 + \cos^2 \psi} \right] + \frac{1}{\gamma} \left[ \frac{1 + \cos^2 \psi}{1 + \cos^2 \psi} \right] + \frac{1}{\gamma} \left[ \frac{1 + \cos^2 \psi}{1 + \cos^2 \psi} \right] + \frac{1}{\gamma} \left[ \frac{1 + \cos^2 \psi}{1 + \cos^2 \psi} \right] + \frac{1}{\gamma} \left[ \frac{1 + \cos^2 \psi}{1 + \cos^2 \psi} \right] + \frac{1}{\gamma} \left[ \frac{1 + \cos^2 \psi}{1 + \cos^2 \psi} \right] + \frac{1}{\gamma} \left[ \frac{1 + \cos^2 \psi}{1 + \cos^2 \psi} \right] + \frac{1}{\gamma} \left[ \frac{1 + \cos^2 \psi}{1 + \cos^2 \psi} \right] + \frac{1}{\gamma} \left[ \frac{1 + \cos^2 \psi}{1 + \cos^2 \psi} \right] + \frac{1}{\gamma} \left[ \frac{1 + \cos^2 \psi}{1 + \cos^2 \psi} \right] + \frac{1}{\gamma} \left[ \frac{1 + \cos^2 \psi}{1 + \cos^2 \psi} \right] + \frac{1}{\gamma} \left[ \frac{1 + \cos^2 \psi}{1 + \cos^2 \psi} \right] + \frac{1}{\gamma} \left[ \frac{1 + \cos^2 \psi}{1 + \cos^2 \psi} \right] + \frac{1}{\gamma} \left[ \frac{1 + \cos^2 \psi}{1 + \cos^2 \psi} \right$$

$$\frac{\partial R(\psi, t)}{\partial \psi} = \frac{t \nu_0 F'(\psi)}{\pm t \gamma (\nu_0 F(\psi) - w) + 1} + R_0 F'(\psi) \tag{16}$$

Based on the expression of  $\frac{\partial R(\psi,t)}{\partial \psi}$  along time and its relationship with zero, it can be concluded that: the closer to the apex, the greater the radial distance would be, and thus the point where  $\psi = 0$  (the apex of the CME) always remains at the forefront of the CME.

The distance  $(\Delta R(t))$  from the point on the CME flank  $(\psi = \psi')$ to the apex ( $\psi = 0$ ) is:

$$\Delta R(t) = R(0,t) - R(\psi',t) = \pm \frac{1}{\gamma} \ln \frac{1 \pm \gamma(\nu_0 - w)t}{1 \pm \gamma(\nu_0 F(\psi') - w)t} + R_0(1 - F(\psi'))$$
(17)

The asymptotic constant form of  $\Delta R(t)$  is  $\lim_{t\to\infty} \Delta R(t) \approx \pm \frac{1}{y} \ln \frac{v_0 - w}{v_0 F(\psi') - w} + R_0 (1 - F(\psi'))$ , which is attained earlier with larger value of  $\gamma$ .

From the expression of  $v(\psi,t)$ , we find that  $v(\psi) = w$  when  $t \to \infty$ , and thus  $\Delta v(t) = v(0,t) - v(\psi',t) \to 0$ . Consequently, each point on the CME front with different initial speeds will eventually approach the solar wind speed.

### 3.2.2 DBEM

DBEM (Dumbović et al., 2018) adopts the geometry of the CME front proposed in the LSF-DBM, which is a cone that gradually flattens out. DBEM employs an ensemble method to account for the uncertainties in the DBM parameters to address the limitation of insufficient reliable input data for the CME prediction, obtaining the most likely arrival time and propagation speed upon arrival of the corresponding ICME.

For the input parameters, n distinct measurement sets are employed for the CME's initial parameters, and the synthetic values are adopted for w and y. The mathematical derivation

processes for obtaining the m synthetic values are as follows (Equations 18, 19):

Assuming that the real measurements of w and  $\gamma$  follow a normal distribution, thus  $x = \overline{x} \pm \Delta x$ , where  $\overline{x} = \mu$  is the mean of the normal distribution, and  $\Delta x = 3 \cdot \sigma$ . Then, normalizing the random variable x through the transformation  $z = \frac{x-\mu}{\sigma}$  makes z follow the standard normal distribution:

$$g(z) = \frac{1}{2} \left( 1 + \operatorname{erf}\left(\frac{z}{\sqrt{2}}\right) \right) \tag{18}$$

where  $\operatorname{erf}(z) = \frac{2}{\sqrt{\pi}} \int_0^z \mathrm{e}^{-y^2} \mathrm{d}y$ . Multiplying both sides of Equation 18 by m-1 will result in g \* (z) = (m-1)g(z), then

$$z_i = -\sqrt{2} \operatorname{erf}^{-1} \left( 1 - 2 \frac{g_i^*(z)}{m-1} \right)$$
 (19)

where  $g_i * (z) = 0, 1, 2, ..., m - 2, m - 1$ . Thus m synthetic values can be obtained. The complete derivations for the formulas are available in the cited references (Dumbović et al., 2018).

By substituting  $n \cdot m^2$  sets of the input parameters into Equations 14, 15, the DBM is run for  $n \cdot m^2$  times to generate an ensemble of the CME's arrival times and propagation speeds. In this way, we can obtain the most likely arrival time of the CME and its propagation speed upon arrival along with their associated uncertainties.

#### 3.2.3 DBEMv3, DBEMv4

Čalogović et al. (2021) sorted out the development process from the original DBEM to its third-generation version (DBEMv3). The DBEMv1 was established by replacing all input parameters in DBEM with the aforementioned synthetic values. Subsequently, under the assumption that the input parameters follow a normal distribution, they drew random samples from the distribution with the number of samples equal to the number of times of running DBEM, thus yielding DBEMv2. After that, the actual motion state of the target is considered during the propagation of CME, more targets are added, and the calculating speed is increased, which lead to the DBEMv2.5 model. Then, the visualization of DBMv2.5 is enhanced through the integration of the existing DBM tools. Additionally, the model can optionally incorporate the Graduated Cylindrical Shell (GCS) model to calculate the CME's half angular width ( $\lambda$ ). As a result, the DBEMv3 model is obtained. In 2022, a Solar Wind (SW) module was added to the model, allowing users to run the DBEM in multiple steps, resulting in DBEMv4. The mathematical expressions for  $\lambda$  derived from the GCS model are given by:

$$k = \sin(\delta)$$

$$\omega_{FO}=2(\alpha+\delta)$$

$$\omega_{EO} = 2\delta$$

$$\lambda = \omega_{FO} - (\omega_{FO} - \omega_{EO})(|\gamma|/90)$$

where  $\alpha$ , k, and  $\gamma$  are the input parameters of GCS model. Additional details can be found in the cited references (Čalogović et al., 2021).

#### 3.3 PDBM series

Napoletano et al. (2018) proposed the PDBM model to address the issue of the lack of the CME information. Subsequently, Napoletano et al. (2022) made improvements to it. Recently, Chierichini et al. (2024) and Mugatwala et al. (2024) further developed this model.

#### 3.3.1 PDBM

The 2018 PDBM (Napoletano et al., 2018) replaced the constant input parameters ( $R_0$ ,  $v_0$ , w, and y) of the DBM with the probability distribution functions (PDFs) of the input parameters. For  $R_0$  and  $v_0$ , the PDFs are determined such that their mean values are the distance and speed obtained by the CME tracking, respectively. The standard deviations are the uncertainties related to these measurements. For w and y, the PDFs are determined by using the selected CME event data, solving the analytical solutions of the DBM in reverse to obtain the values of w and y, thereby obtaining the distribution histograms of the two parameters. Then, the normal distribution function is used to fit the histogram of the background solar wind speed distribution, and the Log-Normal function is used to fit the histogram of the drag parameter distribution. The mathematical derivation processes for solving the analytical solutions of the DBM in reverse are as follows:

The analytical solutions proposed in the DBM are transformed into

$$\gamma = \frac{\nu_0 - \nu_{1AU}}{(\nu_0 - w)(\nu_{1AU} - w)t_{1AU}}$$
 (20)

$$\frac{(v_0 - w)(v_{1AU} - w)t_{1AU}}{v_0 - v_{1AU}} \ln \left[ \frac{v_0 - v_{1AU}}{v_{1AU} - w} + 1 \right] + wt_{1AU} + R_0 - R_{1AU} = 0$$
(21)

where  $R_0$ ,  $v_0$ , the arrival time of ICME at 1AU ( $t_{1AU}$ ), and the propagation speed of ICME at 1AU ( $\nu_{1\mathrm{AU}}$ ) are the known quantities. Solve Equation 21 numerically to obtain the value of w, and then substitute it into Equation 20 to obtain the value of  $\gamma$ .

Subsequently, n initial condition sets are sampled from the obtained distribution functions of these parameters  $R_0$ ,  $v_0$ , w and y, and substituted into the analytical solutions of the DBM. Using the ensemble method, the PDFs of the arrival time and the propagation speed at the target location are generated. The best estimates of both arrival time and propagation speed as well as their corresponding error estimates are the mean and the root mean square of the obtained PDFs, respectively.

The PDBM in 2022 (Napoletano et al., 2022) employed an expanded ICME dataset to establish the new empirical probability distribution functions (PDFs) for the model's input parameters, where the drag parameter's distribution maintains a log-normal functional form, but is categorized into two cases,  $v_0 < w$  and  $v_0 >$ 

The PDBM proposed by Chierichini et al. (2024) improved the model by enhancing the distribution functions of the input parameters through the use of a Monte Carlo Markov Chains method. Also in 2024, Mugatwala et al. (2024) developed the 2022 PDBM by using pairwise selection for the initial speed ( $v_0$ ) and the transit time ( $t_{1AU}$ ) to explore the samples with a lower probability in the parameter space, restricting values of w and y, and selecting the CMEs suitable for the DBM inversion according to the acceptance rate (AR = the number ratio of the feasible solutions under restricted conditions to the total solutions) to obtain the most suitable PDFs for w and  $\gamma$ .

### 3.3.2 The relationship between the mathematical expressions in the PDBM series

The PDBM in 2018, relative to the DBM, obtains the expressions for the drag parameter and the background solar wind speed by inverting the analytical solutions proposed in the DBM. The background solar wind speed from the numerical solution can be input to the equation to calculate the drag parameter. Furthermore, the model also uses the analytical solutions proposed in the DBM to calculate the arrival time of CME and its propagation speed upon arrival.

Compared with the PDBM in 2018, the equations for calculating the drag parameter, background solar wind speed, CME arrival time, and propagation speed in the 2022 PDBM remain unchanged. The mathematical relationship between the two 2024 PDBMs and the 2022 PDBM is the same as that between the 2018 and 2022 PDBMs.

### 3.4 ExDBM

Knowing that the general DBM models account for only the drag force and thus cannot depict appropriately the complex dynamical interactions between CMEs and the ambient solar wind, Rossi et al. (2025) introduced the ExDBM model. ExDBM addresses the limitations inherent to the 2013 version of the DBM through the incorporation of an additional acceleration term (a'). This acceleration term represents the other forces involved in the dynamic interaction between the CME and the solar wind, enabling a more accurate modeling of the CME's propagation dynamics in the heliosphere.

The form of the ExDBM is:

$$\ddot{R} = -\gamma |\dot{R} - w| (\dot{R} - w) + a' \tag{22}$$

The asymptotic constant solution of the model is  $v = w \pm$  $\sqrt{\pm a'/\gamma}$ . When a' < 0, the sign takes "-"; when a' > 0, it takes "+".

The processes for solving Equation 22 are as follows (Equations 23–38):

When  $v_0, v(t) \le w$ ,  $\ddot{R} = \gamma(v(t) - w)^2 + a'$ . Therefore,  $\frac{\mathrm{d}(\frac{\mathrm{d}R}{\mathrm{d}t})}{\mathrm{d}t} = a' + \gamma(v(t) - w)^2$ . Thus  $\frac{\mathrm{d}v}{a' + \gamma(v(t) - w)^2} = \mathrm{d}t$ .

When a' > 0, we assume that u = v' - w, thus  $\mathrm{d}v' = \mathrm{d}u$ .

Therefore,  $\int_{v_0}^v \frac{\mathrm{d}v'}{a' + \gamma(v' - w)^2} = \int_{v_0 - w}^{v - w} \frac{\mathrm{d}u}{a' + \gamma u^2} = t, \qquad \frac{1}{\sqrt{a'\gamma}} \arctan\left(\frac{\sqrt{\gamma}u}{\sqrt{a'}}\right)$ 

$$\begin{vmatrix} v - w \\ v_0 - w \end{vmatrix} = t. \text{ Thus}$$

$$t = \frac{1}{\sqrt{a'\gamma}} \left( \arctan\left(\sqrt{\frac{\gamma}{a'}}(\nu - w)\right) - \arctan\left(\sqrt{\frac{\gamma}{a'}}(\nu_0 - w)\right) \right)$$
 (23)

Equation 23 can be transformed into  $\sqrt{a'\gamma}t = \arctan\left(\sqrt{\frac{\gamma}{a'}}(v-w)\right) - \arctan\left(\sqrt{\frac{\gamma}{a'}}(v_0-w)\right)$ . Assuming  $\sigma_+ = \frac{1}{2}$  $\arctan\left(\sqrt{\frac{\gamma}{a'}}(w-v_0)\right)$ , it follows that  $\sqrt{a'\gamma}t = \arctan\left(\sqrt{\frac{\gamma}{a'}}(v-w)\right) +$  $\sigma_+$ , and consequently

$$v(t) = w + \sqrt{\frac{a'}{\gamma}} \tan\left(\sqrt{a'\gamma}t - \sigma_{+}\right), 0 \le t \le \frac{1}{\sqrt{a'\gamma}} \sigma_{+}$$
 (24)

Integrating this expression, we obtain

$$R(t) = wt + R_0 - \frac{1}{\gamma} \ln \left( S_+ \cos \left( \sqrt{a' \gamma} t - \sigma_+ \right) \right), 0 \le t \le \frac{1}{\sqrt{a' \gamma}} \sigma_+ \quad (25)$$

where  $S_+ = \sqrt{\frac{a' + y(v_0 - w)^2}{a'}}$ . Similarly, when a' < 0,

$$v(t) = w + \sqrt{-\frac{a'}{\gamma}} \frac{e^{-2\sqrt{-a'\gamma}t}A_{-} + B_{-}}{e^{-2\sqrt{-a'\gamma}t}A_{-} - B}, t \ge 0$$
 (26)

$$R(t) = \left(w - \sqrt{-\frac{a'}{\gamma}}\right)t + R_0 - \frac{1}{\gamma}\ln\left(\frac{A_-e^{-2\sqrt{-a'}\gamma t} - B_-}{2\sqrt{-a'}}\right), t \ge 0 \quad (27)$$

Here,  $A_- = \sqrt{\gamma}(\nu_0 - w) + \sqrt{-a'}$ ,  $B_- = \sqrt{\gamma}(\nu_0 - w) - \sqrt{-a'}$ . When  $\nu_0 < w < \nu(t)$ , a' > 0. Unlike the previous content,

$$\int_{v_0}^{w} \frac{dv'}{a' + \gamma(v' - w)^2} + \int_{w}^{v} \frac{dv'}{a' - \gamma(v' - w)^2} = t$$
 (28)

where  $\int_{v_0}^{w} \frac{\mathrm{d}v'}{a'+\gamma(v'-w)^2} = \frac{1}{\sqrt{a'y}} \arctan\left(\sqrt{\frac{y}{a'}}(w-v_0)\right) = \frac{1}{\sqrt{a'y}}\sigma_+.$  Assuming u=v'-w, it follows that  $\mathrm{d}v'=\mathrm{d}u$ , and the integral in question is transformed to  $\int_0^{v-w} \frac{\mathrm{d}u}{a'-yu^2}.$  Thus,  $\int_0^{v-w} \frac{\mathrm{d}u}{a'-yu^2} = \frac{1}{2\sqrt{a'y}} \ln\left(\frac{\sqrt{a'}+\sqrt{y}u}{\sqrt{a'}-\sqrt{y}u}\right) |_0^{v-w} = \frac{1}{2\sqrt{a'y}} \ln\left(\frac{\sqrt{a'}+\sqrt{y}(v-w)}{\sqrt{a'}-\sqrt{y}(v-w)}\right).$  Therefore,  $t-\frac{1}{\sqrt{a'y}}\sigma_+ = \frac{1}{2\sqrt{a'y}} \ln\left(\frac{\sqrt{a'}+\sqrt{y}(v-w)}{\sqrt{a'}-\sqrt{y}(v-w)}\right).$  Take the exponential functions on both sides of the equation, and we obtain  $\frac{\sqrt{a'}+\sqrt{y}(v-w)}{\sqrt{a'}-\sqrt{y}(v-w)} = \frac{2\sqrt{a'y}\left(t-\frac{1}{\sqrt{a'y}}\sigma_+\right)}{e}.$  Assuming  $k=e^{2\sqrt{a'y}\left(t-\frac{1}{\sqrt{a'y}}\sigma_+\right)}$ , it follows that  $\sqrt{a'}+\sqrt{y}(v-w)=k\left(\sqrt{a'}-\sqrt{y}(v-w)\right),$  and consequently

$$v = w + \frac{k-1}{1+k} \frac{\sqrt{a'}}{\sqrt{\gamma}} = w + \sqrt{\frac{a'}{\gamma}} \frac{e^{2(\sqrt{a'}\gamma t - \sigma_+)} - 1}{e^{2(\sqrt{a'}\gamma t - \sigma_+)} + 1}, t > \frac{1}{\sqrt{a'\gamma}} \sigma_+$$
 (29)

By integrating the preceding equation, we obtain

$$R(t) = \left(w - \sqrt{\frac{a'}{\gamma}}\right)t + R_0 + \frac{1}{\gamma}\left(\ln\left(\frac{e^{2\left(\sqrt{a'\gamma}t - \sigma_+\right)} + 1}{2S_+}\right) + \sigma_+\right), t > \frac{1}{\sqrt{a'\gamma}}\sigma_+$$
(30)

In summary, when a' > 0, if  $v_0 \le w$ , then

$$v(t) = \begin{cases} w + \sqrt{\frac{a'}{\gamma}} \tan\left(\sqrt{a'\gamma}t - \sigma_{+}\right), 0 \le t \le \frac{1}{\sqrt{a'\gamma}} \sigma_{+} \\ w + \sqrt{\frac{a'}{\gamma}} \frac{e^{2\left(\sqrt{a'\gamma}t - \sigma_{+}\right)} - 1}{e^{2\left(\sqrt{a'\gamma}t - \sigma_{+}\right)} + 1}, t > \frac{1}{\sqrt{a'\gamma}} \sigma_{+} \end{cases}$$

$$R(t) = \begin{cases} wt + R_{0} - \frac{1}{\gamma} \ln\left(S_{+} \cos\left(\sqrt{a'\gamma}t - \sigma_{+}\right)\right), 0 \le t \le \frac{1}{\sqrt{a'\gamma}} \sigma_{+} \\ \left(w - \sqrt{\frac{a'}{\gamma}}\right) t + R_{0} + \frac{1}{\gamma} \left(\ln\left(\frac{e^{2\left(\sqrt{a'\gamma}t - \sigma_{+}\right)} + 1}{2S_{+}}\right) + \sigma_{+}\right), \quad (32) \\ t > \frac{1}{\sqrt{a'\gamma}} \sigma_{+} \end{cases}$$

Here, 
$$\sigma_+ = \arctan\left(\sqrt{\frac{\gamma}{a'}}(w - v_0)\right)$$
,  $S_+ = \sqrt{\frac{a' + \gamma(v_0 - w)^2}{a'}}$ .

When a' < 0, if  $v_0 \le w$ , then

$$v(t) = w + \sqrt{-\frac{a'}{\gamma}} \frac{e^{-2\sqrt{-a'\gamma}t}A_{-} + B_{-}}{e^{-2\sqrt{-a'\gamma}t}A_{-} - B_{-}}, t \ge 0$$
(33)

$$R(t) = \left(w - \sqrt{-\frac{a'}{y}}\right)t + R_0 - \frac{1}{y}\ln\left(\frac{A_-e^{-2\sqrt{-a'}yt} - B_-}{2\sqrt{-a'}}\right), t \ge 0 \quad (34)$$

where  $A_{-} = \sqrt{y}(v_0 - w) + \sqrt{-a'}$ ,  $B_{-} = \sqrt{y}(v_0 - w) - \sqrt{-a'}$ .

By replacing the plus and minus signs in Equations 31–34, we can obtain:

When a' > 0, if  $v_0 > w$ , then

$$\nu(t) = w + \sqrt{\frac{a'}{\gamma}} \frac{e^{2\sqrt{a'\gamma}t} A_{+} + B_{+}}{e^{2\sqrt{a'\gamma}t} A_{+} - B_{+}}, t \ge 0, \tag{35}$$

$$R(t) = \left(w - \sqrt{\frac{a'}{\gamma}}\right)t + R_0 + \frac{1}{\gamma}\ln\left(\frac{A_+ e^{2\sqrt{a'}\gamma t} - B_+}{2\sqrt{a'}}\right), t \ge 0.$$
 (36)

Here,  $A_+=\sqrt{\gamma}(\nu_0-w)+\sqrt{a'}$  and  $B_+=\sqrt{\gamma}(\nu_0-w)-\sqrt{a'}$ . When a'<0, if  $\nu_0>w$ , then

$$v(t) = \begin{cases} w - \sqrt{-\frac{a'}{\gamma}} \tan\left(\sqrt{-a'\gamma}t - \sigma_{-}\right), 0 \le t \le \frac{1}{\sqrt{-a'\gamma}} \sigma_{-} \\ w + \sqrt{-\frac{a'}{\gamma}} \frac{e^{-2\left(\sqrt{-a'\gamma}t - \sigma_{-}\right)} - 1}{e^{-2\left(\sqrt{-a'\gamma}t - \sigma_{-}\right)} + 1}, t > \frac{1}{\sqrt{-a'\gamma}} \sigma_{-} \end{cases}$$

$$R(t) = \begin{cases} wt + R_{0} + \frac{1}{\gamma} \ln\left(S_{-}\cos\left(\sqrt{-a'\gamma}t - \sigma_{-}\right)\right), 0 \le t \le \frac{1}{\sqrt{-a'\gamma}} \sigma_{-} \\ \left(w - \sqrt{-\frac{a'}{\gamma}}\right)t + R_{0} - \frac{1}{\gamma} \left(\ln\left(\frac{e^{-2\left(\sqrt{-a'\gamma}t - \sigma_{-}\right)} + 1}{2S_{-}}\right) - \sigma_{-}\right), t \\ > \frac{1}{\sqrt{-a'\gamma}} \sigma_{-} \end{cases}$$

where  $\sigma_{-} = \arctan\left(\sqrt{-\frac{\gamma}{a'}}(v_0 - w)\right)$ ,  $S_{-} = \sqrt{\frac{a' - \gamma(v_0 - w)^2}{a'}}$ .

#### 3.5 EnDBM series

### 3.5.1 EnDBM

Employing the remote-sensing observations of STEREO, Hess and Zhang (2014) independently tracked the evolution of not only the CME front but also the associated shock front. By fitting the evolution of these two fronts to the DBM, they predicted the in situ arrival of both the CME and the shock, thereby developing the DBM further and proposing the EnDBM. In this approach, geometric structures are superimposed onto images captured by different spacecraft at approximately the same time using the forward modeling technology. Optimal parameters are then determined to ensure the consistency between the model images and the multiview observations. Where the CME front uses the GCS model and direct images, while the shock front uses the prolate spheroid bubble model and the running-difference images. These geometric models were applied to the given events along multiple time steps, yielding a series of height-time measurements for both the CME and shock. Subsequently, the DBM was used to fit the time-height data of both fronts obtained through the forward modeling, determining the sole

(38)

TABLE 1 The reference, key features, basic assumptions and limitations of the DBM family models. w stands for the speed of the background solar wind, and y stands for the drag parameter. Y indicates Yes, N indicates No.

Model	References	Key features	Basic ass	umptions	Limita	ations
			w = const y = const	Geometry	Reliance on idealized assumptions	Cannot be applied to interacting ICMEs
DBM	Vršnak et al. (2013)	geometry- independent	Y	N	Y	Y
ELEvo	Möstl et al. (2015)	DBM + a self similar expanding ellipse	Y	self similar expanding ellipse	Y	Y
ELEvoHI	Rollett et al. (2016)	HI observations + FPF method + ElCon method + DBM fitting + ELEvo	Y	self similar expanding ellipse (ElCon method, ELEvo)	Y	Y
	Braga et al. (2020)	data from two perspectives of the HI-1 on STEREO A and STEREO B+ ElCon method + DBM	N ( $w \neq \text{const}, y \neq \text{const}$ )	self similar expanding ellipse (ElCon method)	Y	Y
ELEvoHI ensemble model	Amerstorfer et al. (2018)	ELEvoHI (2016) + GCS + ensemble method	Y	self similar expanding ellipse (ELEvoHI)	Y	Y
ELEvoHI 2.0	Hinterreiter et al. (2021)	ELEvoHI ensemble model + deformed CME front	N ( $w \neq \text{const}, y \neq \text{const}$ )	deformed CME front (outside the DBM fitting range)	Y	Y
LSF-DBM	Žic et al. (2015), Sudar et al. (2022)	DBM + a self-similar cone; DBM + a flattening cone	Y	self-similar cone, flattening cone	Y	Y
DBEM	Dumbović et al. (2018)	DBM with a flattening cone + ensemble method + the synthetic values are adopted for w and y	Y	flattening cone	Y	Y
DBEMv1	Čalogović et al. (2021)	DBEM + all input parameters in DBEM use the synthetic values	Y	flattening cone	Y	Y
DBEMv2	Čalogović et al. (2021)	DBEM + random samples from the distribution of input parameters	Y	flattening cone	Y	Y
DBEMv2.5	Čalogović et al. (2021)	DBEMv2 + actual motion state of the target + more targets + increased calculation speed	Y	flattening cone	Y	Y
DBEMv3	Čalogović et al. (2021)	DBEMv2.5 + optional GCS model	Y	flattening cone	Y	Y
DBEMv4		DBEMv3 + Solar Wind (SW) module	N ( $w \neq \text{const}$ )	flattening cone	Y	Y

(Continued on the following page)

TABLE 1 (Continued) The reference, key features, basic assumptions and limitations of the DBM family models. w stands for the speed of the background solar wind, and y stands for the drag parameter. Y indicates Yes, N indicates No.

Model	References	Key features	Basic ass	umptions	Limitations	
			w = const y = const	Geometry	Reliance on idealized assumptions	Cannot be applied to interacting ICMEs
PDBM	Napoletano et al. (2018), Napoletano et al. (2022)	DBM + ensemble method	Y	N	Y	Y
PDBM	Chierichini et al. (2024)	DBM + ensemble method + Monte Carlo Markov Chains method	Y	N	Y	Y
PDBM	Mugatwala et al. (2024)	DBM + ensemble + pairwise selection method	Y	N	Y	Y
ExDBM	Rossi et al. (2025)	DBM + additional acceleration term	Y	N	Y	Y
EnDBM	Hess and Zhang (2014)	DBM + GCS + the prolate spheroid bubble model	Y	GCS (CME front), the prolate spheroid bubble model (shock front)	Y	Y
EnDBM	Hess and Zhang (2015)	DBM + GCS + the prolate spheroid bubble model + geometric corrections to the propagation direction	N (y ≠ const)	GCS (CME front), the prolate spheroid bubble model (shock front)	Y	Y

unknown parameter ( $\gamma$ ), and ultimately deriving the equations of motions for both the CME and the shock.

Hess and Zhang (2015) further refined the EnDBM by (1) changing the drag parameter to a variable one, (2) implementing the geometric corrections to the propagation direction, and (3) developing a new shock propagation prediction model. The changing drag parameter is calculated as:

$$\gamma = \frac{C_{\rm d}}{\frac{\rho_0 k R_0}{\rho_{w0}} + \frac{kR}{2}}$$
 (39)

where  $C_{\rm d}$  and k are the known dimensionless parameters, which are 1.35 and 0.4, respectively. In Equation 39, only the density ratio is an unknown quantity. Through the forward modeling technique used in the EnDBM in 2014, multiple sets of the height-time data measured during the CME propagation are obtained. A series of fits are performed to these data to estimate the value of  $\gamma$  for each time. Subsequently, a series of the discrete  $\gamma$  values obtained by fitting with Equation 39 were used with an optimization algorithm to determine the density ratio  $(\rho_0/\rho_{\rm w0})$ , thereby defining the complete  $\gamma$ ( $\gamma$ ) function. The specific derivation processes of  $\gamma$  can be found in the reference (Hess and Zhang, 2015).

By combining measurements of the ejecta front and the sheath front, the proposed model predicts the sheath propagation through the motion equations:  $R_{SF}(t) = R_{FR}(t) + At + B$  and  $v_{SF}(t) = v_{FR}(t) + A$ , where A and B are the coefficients for the linear fitting of the distance of the ejecta front and the sheath front, respectively. The propagation of the sheath is geometrically corrected using the same method for the CME.

## 4 Other DBM models

In addition to the series of models evolving based on the basic version of the DBM, there are also some DBMs without a clear development route, such as the Graduated Cylindrical Shell Drag-Based Model (GCSDBM), the mass-changing Drag-Based Model (mass-changing DBM).

# 4.1 GCSDBM

Shi et al. (2015) employed the GCS model fitting to determine the CME's initial speed, as this method ensures that the derived speed remains unaffected by the projection effects. Then they utilized the DBM to establish the relationship between the CME's transit time and its initial speed, which yields the GCSDBM. The expressions of the DBM are:

TABLE 2 The input and output parameters of the DBM family models.  $t_0$  stands for the initial time of the CME,  $v_0$  stands for the initial speed of the CME,  $r_0$  stands for the initial radial distance of the CME, w stands for the speed of the background solar wind, y stands for the drag parameter,  $\lambda$  stands for the half angular width of the CME,  $\phi$  stands for the propagation direction of the CME, and f stands for the inverse aspect ratio of the CME. Y indicates Yes, N indicates No.

Model	Input parameters					Output parameters	
	t <sub>0</sub> , v <sub>0</sub> , r <sub>0</sub> , w, γ, distance to the target	λ, φ	f	Optional GCS parameters	Associated uncertainties of the CME's initial parameters	Transit time and propagation speed of CME	Associated uncertainties of the CME's transit time and propagation speed
DBM	Y	N	N	N	N	Y	N
ELEvo	Y	Y	Y	N	N	Y	N
ELEvoHI	Y	Y	Y	N	N	Y	N
ELEvoHI ensemble model	Y	Y	Y	N	$Y(\phi,\lambda,f)$	Y	Y
ELEvoHI 2.0	Y	Y	Y	N	$Y(\phi,\lambda,f)$	Y	Y
LSF-DBM	Y	Y	N	N	N	Y	N
DBEM	Y	Y	N	N	Υ (w, γ)	Y	Y
DBEMv1	Y	Y	N	N	$\begin{array}{c} \mathrm{Y}\;(t_0, \nu_0, w, \\ \gamma, \lambda, \phi) \end{array}$	Y	Y
DBEMv2	Y	Y	N	N	$\begin{array}{c} \mathrm{Y}\;(t_0, \nu_0, w, \\ \gamma, \lambda, \phi) \end{array}$	Y	Y
DBEMv2.5	Y	Y	N	N	$\begin{array}{c} \mathrm{Y}\;(t_0, \nu_0, w, \\ \gamma, \lambda, \phi) \end{array}$	Y	Y
DBEMv3	Y	Y	N	Y	$\begin{array}{c} \mathrm{Y}\;(t_0,\nu_0,w,\\ \gamma,\lambda,\phi) \end{array}$	Y	Y
DBEMv4	Y	Y	N	Y	$\begin{array}{c} \mathrm{Y}\;(t_0, \nu_0, w, \\ \gamma, \lambda, \phi) \end{array}$	Y	Y
PDBM	Y	N	N	N	Y	Y	Y
ExDBM	Y	N	N	N	N	Y	N
EnDBM	Y	N	N	N	N	Y	N

Based on the equation  $\frac{\mathrm{d}v}{\mathrm{d}t} = -\gamma(v-w)|v-w|^{\beta-1}$ , it can be obtained that  $R_\beta = wt \pm \frac{1}{\gamma(2-\beta)} \left\{ |v_0-w|^{2-\beta} - \left[\gamma(\beta-1)t + |v_0-w|^{1-\beta}\right]^{\frac{2-\beta}{1-\beta}} \right\}$  when  $1 < \beta < 2$ . For  $\beta = 1$ ,  $R_1 = wt + \frac{1}{\gamma}(v_0-w)(1-e^{-\gamma t})$ . For  $\beta = 2$ ,  $R_2 = wt \pm \frac{1}{\gamma} \ln{(\gamma|v_0-w|t+1)}$ . When  $v_0 > w$ , the sign takes "+"; when  $v_0 < w$ , it takes "-". Then, by using the fitting method and the above relationships, the parameters  $\gamma$ ,  $\beta$ , and w can be derived from the existing measurements of the initial speed and the transit time. Subsequently, the transit time of the CME to 1 AU can be determined with the known parameter  $v_0$  derived from the GCS model.

# 4.2 The mass-changing DBM

Stamkos et al. (2023) proposed the mass-changing DBM for modeling the propagation of fast CMEs in the inner heliosphere, which improved the prediction accuracy of their arrivals at 1 AU. Compared with the previous models, this version considers: (1) the virtual mass of CMEs, and (2) the CME's magnetic erosion caused by the reconnection between the CME and the interplanetary magnetic field (IMF).

This model adopts a cylindrical geometry of CME with radial propagation in the inner heliosphere. The expression satisfied by the non-erosive fast CME subject to the drag force  $(F_{\rm drag})$  is

$$\frac{\mathrm{d}v}{\mathrm{d}t} = -\gamma C_{\mathrm{d}} |v - w| (v - w) - \frac{\left(v + V_{\mathrm{exp}} - w\right)}{M_{\mathrm{tot}}} \frac{\mathrm{d}M_{\mathrm{v}}}{\mathrm{d}t} \tag{40}$$

where  $\gamma = \frac{\rho_w A}{V(\rho + \frac{\rho_w}{2})} = \frac{4}{\pi R(\frac{2\rho}{\rho_w} + 1)}$ ,  $M_{\text{tot}} = M + M_v$ ,  $\nu$  is the speed of the

CME, w is the background solar wind speed,  $V_{\rm exp}$  is the expansion speed of the CME,  $\rho$  is the density of the CME,  $\rho_{\rm w}$  is the density of the background solar wind,  $M_{\rm tot}$  is the total mass, M is the mass of the CME,  $M_{\rm v}$  is the virtual mass, V is the volume of the CME, R is the radius of the CME, and A is the cross-sectional area of the CME. Assuming that M remains constant, it can be seen that  $M_{\rm tot}$  varies with the CME's propagation distance.

Subsequently, by reducing the radius of the CME, the influence of the magnetic erosion is incorporated into the motion of the CME (i.e., Equation 40):  $R_i = R_{i-1}^* \left(\frac{\mathfrak{R}_i}{\mathfrak{R}_{i-1}}\right)^{\alpha}$ , where  $\mathfrak{R}_i = C'S$  is a hybrid magnetic-reconnection rate, C' is a dimensionless coefficient, which is approximately 0.1,  $S = 2(B_1B_2)^{\frac{3}{2}} \left(\mu_0\rho_1B_2 + \mu_0\rho_2B_1\right)^{-\frac{1}{2}}(B_1 + B_2)^{-\frac{1}{2}}$ , B is the magnetic field intensity, subscript 1 represents CME, subscript 2 represents the solar wind and IMF at the position of the CME front, and  $\mu_0$  represents the magnetic permeability of vacuum. The specific derivation and solution processes of the mass-changing DBM can be found in the reference (Stamkos et al., 2023).

# 5 Conclusion

This paper systematically reviews the development and evolution of the DBM models. The DBM assumes that the CME is only subject to the drag force in its later propagation stage. It describes the propagation of CMEs in the interplanetary medium (solar wind) based on the motion equations determined by the drag force, and is used to predict the transit time and propagation speed of the CME at Earth or any given target in the solar system. It is one of the most widely employed analytical models, due to its simplicity and computational efficiency. Furthermore, this paper also presents the mathematical derivation processes of each version of the DBM, sorts out the development and evolution processes as well as the interrelationships between the mathematical expressions of different versions of the DBM, and proposes the potential improvement directions for some evolution routes. According to our compilation, the development and evolution of the DBM models can be categorized into five development routes: DBM → ELEvoHI model series; DBM → LSF-DBM series; DBM → PDBM series;  $DBM \rightarrow ExDBM$ ;  $DBM \rightarrow EnDBM$  series. In addition, some DBMwithout a clear development route are also introduced, including the GCSDBM and the mass-changing DBM. As a summary, Tables 1, 2 list the key features of each model, including the assumptions, inputs, outputs, limitations and so on, for a detailed comparison.

The ELEvo model treats the CME shape as a self-similar ellipse. Based on the analytical solutions of the DBM, it derives the distance and speed equations at any point of the CME front. The ELEvo model was used in the subsequent development of the ELEvoHI model. Furthermore, the ELEvoHI model is improved by combining the ensemble method, introducing the deformed CME front, the

varying drag parameter, and the varying background solar wind speed. In the future, the inverse aspect ratio in the ELEvo model can be developed as a function of time, using more realistic solar wind conditions instead of empirical expressions, and considering the mass-changing of the CME over time to further improve the model.

The LSF-DBM treats the CME geometry as either a self-similar cone or a flattening cone. Similar to the ELEvo model, it employs the analytical solutions of the DBM to derive the distance and speed equations at any point of the CME front. In the subsequently developed DBEM, the flattening conical geometry equation proposed in the LSF-DBM is adopted. Future improvements to the model may include incorporating a sophisticated drag parameter model.

The PDBM employs the DBM's analytical solutions to calculate the CME's arrival time and speed, and obtains the values of the drag parameter and the background solar wind speed by inversely solving the analytical solutions. In the future, the model can be improved by adding two-dimensional geometric models (conical or elliptical shapes), or by further exploring the Bayesian method.

The ExDBM improves the model by adding an acceleration term to the DBM. This term represents other forces in the dynamic interaction between the CME and the solar wind, enabling more accurate modeling of the CME's propagation dynamics in the heliosphere.

In the EnDBM, the CME geometry is modeled using the GCS model, while the shock geometry is modeled using a prolate spheroid bubble model. The model employs the DBM's analytical solutions to fit the measured height-time data, deriving the CME's motion equations to predict the *in situ* arrival of both the CME flux rope and the sheath. A variable drag parameter is then applied, and the GCS model's results undergo the geometric correction. A new model is used to predict the propagation of the sheath.

We have to admit that the various versions of the DBM family models have their own some limitations. These limitations include, but are not limited to the idealized assumptions, sensitivity to the initial conditions of both CME and solar wind. These assumptions, on one hand, come from the idealized geometries of the CME front shape, which could be very complicated in real cases. On the other hand, they come from the negligence of other forces besides the drag force exerted by the background solar wind. Especially, none of the various DBM-based models discussed above explicitly takes into account the deflection of CMEs during their propagation. However, the CME deflection is known to be an important factor influencing not only the prediction accuracy of the CME arrival time but also the success rate of whether a CME can reach the Earth or a given target location at all (Wang et al., 2004; Gui et al., 2011; Zhuang et al., 2019). The lack of the deflection treatment in current DBM models hinders the improvement of the model's accuracy. In addition to these, the DBM models do not consider the interactions of multiple CMEs.

In the future, these improvements can be implemented to further develop the DBM and enhance its prediction accuracy for the CME arrival time and propagation speed. The models can be better validated if we could have more accurate observations for CMEs (e.g., with radial ICME lineup observations) and incorporate the deflection effects of CMEs. In addition to the improved accuracy

of the CME initial conditions, which can be obtained by regular multi-viewpoint imaging by missions like ESA Vigil in combination with missions at L1, we need to improve the ambient wind models to improve the arrival time and speed forecasts of CMEs, as they are also the key factors concerning the prediction of the CME's kinematics. Besides, we can compare the prediction results of different versions of the DBM for the same specific CME-ICME events. These comparisons can not only verify whether advanced models can give better predictions, but also reveal which factors are important in the modeling. They will be implemented in the next work.

#### **Author contributions**

XZ: Supervision, Writing – review and editing, Writing – original draft, Resources, Funding acquisition. CS: Validation, Visualization, Writing – original draft. XL: Writing – review and editing. XF: Supervision, Writing – review and editing. YZ: Writing – review and editing, Supervision. NX: Writing – review and editing. LD: Writing – review and editing. AK: Writing – review and editing. CM: Supervision, Writing – review and editing.

# **Funding**

The author(s) declare that financial support was received for the research and/or publication of this article. The author(s) declare that this work is jointly supported by the National Natural Science Foundation of China (grant Nos. 42474224, 12203054, 12373059, 12463009), the Beijing Natural Science Foundation (1242035), the Specialized Research Fund for State Key Laboratories, the "Yunnan Revitalization Talent Support Program" Innovation Team Project (grant No. 202405AS350012), and the Yunnan Fundamental Research Projects (grant No. 202301AV070007). This work is supported by ERC grant (HELIO4CAST, 10.3030/101042188). Funded by the European Union. Views and opinions expressed are however those of the author(s) only and do not necessarily reflect those of the European Union or the European Research Council Executive Agency. Neither the European Union nor the granting authority can be held responsible for them. AK acknowledges financial support from the Ministry of Science and Higher Education of the Russian Federation.

## Conflict of interest

The authors declare that the research was conducted in the absence of any commercial or financial relationships that could be construed as a potential conflict of interest.

The reviewer YC declared a past co-authorship with the author(s) XZ and XF to the handling editor.

The author(s) declared that they were an editorial board member of Frontiers, at the time of submission. This had no impact on the peer review process and the final decision.

# Generative AI statement

The author(s) declare that no Generative AI was used in the creation of this manuscript.

Any alternative text (alt text) provided alongside figures in this article has been generated by Frontiers with the support of artificial intelligence and reasonable efforts have been made to ensure accuracy, including review by the authors wherever possible. If you identify any issues, please contact us.

# Publisher's note

All claims expressed in this article are solely those of the authors and do not necessarily represent those of their affiliated organizations, or those of the publisher, the editors and the reviewers. Any product that may be evaluated in this article, or claim that may be made by its manufacturer, is not guaranteed or endorsed by the publisher.

# Supplementary material

The Supplementary Material for this article can be found online at: https://www.frontiersin.org/articles/10.3389/fspas.2025.1686823/full#supplementary-material

# References

Alobaid, K. A., Abduallah, Y., Wang, J. T. L., Wang, H. M., Jiang, H. D., Xu, Y., et al. (2022). Predicting CME arrival time through data integration and ensemble learning. *Front. Astron. Space Sci.* 9, 1013345. doi:10.3389/fspas.2022.1013345

Amerstorfer, T., Möstl, C., Hess, P., Temmer, M., Mays, M. L., Reiss, M. A., et al. (2018). Ensemble prediction of a halo coronal mass ejection using heliospheric imagers. Space weather. 16, 784–801. doi:10.1029/2017SW001786

Boteler, D. H., Pirjola, R. J., and Nevanlinna, H. (1998). The effects of geomagnetic disturbances on electrical systems at the Earth's surface. *Adv. Space Res.* 22, 17–27. doi:10.1016/S0273-1177(97)01096-X

Braga, C. R., Vourlidas, A., Stenborg, G., Dal Lago, A., Mendonça, R. R. S. d., and Echer, E. (2020). Predicting the time of arrival of coronal mass ejections at earth from heliospheric imaging observations. *J. Geophys. Res.* 125, e2020JA027885. doi:10.1029/2020IA027885

Čalogović, J., Dumbović, M., Sudar, D., Vršnak, B., Martinić, K., Temmer, M., et al. (2021). Probabilistic drag-based ensemble model (DBEM) evaluation for heliospheric propagation of CMEs. *Sol. Phys.* 296, 114. doi:10.1007/s11207-021-01859-5

Cargill, P. J. (2004). On the aerodynamic drag force acting on interplanetary coronal mass ejections. Sol. Phys. 221, 135–149. doi:10.1023/b:sola.0000033366. 10725.a2

Chierichini, S., Francisco, G., Mugatwala, R., Foldes, R., Camporeale, E., De Gasperis, G., et al. (2024). A Bayesian approach to the drag-based modelling of ICMEs. *J. Space Weather Space Clim.* 14, 1. doi:10.1051/swsc/2023032

Dumbović, M., Čalogović, J., Vršnak, B., Temmer, M., Mays, M. L., Veronig, A., et al. (2018). The drag-based ensemble model (DBEM) for coronal mass ejection propagation. *Astrophys. J.* 854, 180. doi:10.3847/1538-4357/aaaa66

Dumbović, M., Čalogović, J., Martinić, K., Vršnak, B., Sudar, D., Temmer, M., et al. (2021). Drag-based model (DBM) tools for forecast of coronal mass ejection arrival time and speed. *Front. Astron. Space Sci.* 8, 639986. doi:10.3389/fspas.2021.639986

- Feng, X. S. (2020). Magnetohydrodynamic modeling of the solar corona and heliosphere. Singapore: Springer.
- Feng, X. S., and Zhao, X. H. (2006). A new prediction method for the arrival time of interplanetary shocks. Sol. Phys. 238, 167–186. doi:10.1007/s11207-006-0185-3
- Feng, X. S., Zhou, Y. F., and Wu, S. T. (2007). A novel numerical implementation for solar wind modeling by the modified conservation element/solution element method. *Astrophys. J.* 655, 1110–1126. doi:10.1086/510121
- Feng, X. S., Yang, L. P., Xiang, C. Q., Jiang, C. W., Ma, X. P., Wu, S. T., et al. (2012). Validation of the 3D AMR SIP-CESE solar wind model for four Carrington rotations. *Sol. Phys.* 279, 207–229. doi:10.1007/s11207-012-9969-9
- Fry, C. D., Sun, W., Deehr, C. S., Dryer, M., Smith, Z., Akasofu, S. I., et al. (2001). Improvements to the HAF solar wind model for space weather predictions. *J. Geophys. Res.* 106, 20985–21001. doi:10.1029/2000JA000220
- Gopalswamy, N., Lara, A., Yashiro, S., Kaiser, M. L., and Howard, R. A. (2001). Predicting the 1-AU arrival times of coronal mass ejections. *J. Geophys. Res.* 106, 29207–29217. doi:10.1029/2001JA000177
- Guastavino, S., Candiani, V., Bemporad, A., Marchetti, F., Benvenuto, F., Massone, A. M., et al. (2023). Physics-driven machine learning for the prediction of coronal mass ejections' travel times. *Astrophys. J.* 954, 151. doi:10.3847/1538-4357/ace62d
- Gui, B., Shen, C. L., Wang, Y. M., Ye, P. Z., Liu, J. J., Wang, S., et al. (2011). Quantitative analysis of CME deflections in the corona. *Sol. Phys.* 271, 111–139. doi:10.1007/s11207-011-9791-9
- Hess, P., and Zhang, J. (2014). Stereoscopic study of the kinematic evolution of a coronal mass ejection and its driven shock from the sun to the Earth and the prediction of their arrival times. *Astrophys. J.* 792, 49. doi:10.1088/0004-637X/792/1/49
- Hess, P., and Zhang, J. (2015). Predicting CME ejecta and sheath front arrival at L1 with a data-constrained physical model. *Astrophys. J.* 812, 144. doi:10.1088/0004-637X/812/2/144
- Hinterreiter, J., Amerstorfer, T., Temmer, M., Reiss, M. A., Weiss, A. J., Möstl, C., et al. (2021). Drag-based CME modeling with heliospheric images incorporating frontal deformation: ELEvoHI 2.0. *Space weather.* 19, e2021SW002836. doi:10.1029/2021SW002836
- Kay, C., Palmerio, E., Riley, P., Mays, M. L., Nieves-Chinchilla, T., Romano, M., et al. (2024). Updating measures of CME arrival time errors. *Space weather.* 22, e2024SW003951. doi:10.1029/2024SW003951
- Li, Y. C., Yang, Y., Shen, F., Tang, B. F., and Lin, R. P. (2024). CME arrival time prediction based on coronagraph observations and machine-learning techniques. *Astrophys. J.* 976, 141. doi:10.3847/1538-4357/ad82e5
- Liu, H. L., and Qin, G. (2012). Using soft x-ray observations to help the prediction of flare related interplanetary shocks arrival times at the Earth. *J. Geophys. Res.* 117, A04108. doi:10.1029/2011JA017220
- Liu, J. J., Ye, Y. D., Shen, C. L., Wang, Y. M., and Erdélyi, R. (2018). A new tool for CME arrival time prediction using machine learning algorithms: CAT-PUMA. *Astrophys. J.* 855, 109. doi:10.3847/1538-4357/aaae69
- Minta, F. N., Nozawa, S., Kozarev, K., Elsaid, A., and Mahrous, A. (2023). Forecasting the transit times of earth-directed halo CMEs using artificial neural network: a case study application with GCS forward-modeling technique. *J. Atmos. Sol. Terr. Phys.* 247, 106080. doi:10.1016/j.jastp.2023.106080
- Möstl, C., Rollett, T., Frahm, R. A., Liu, Y. D., Long, D. M., Colaninno, R. C., et al. (2015). Strong coronal channelling and interplanetary evolution of a solar storm up to Earth and Mars. *Nat. Commun.* 6, 7135. doi:10.1038/ncomms8135
- Mugatwala, R., Chierichini, S., Francisco, G., Napoletano, G., Foldes, R., Giovannelli, L., et al. (2024). A catalogue of observed geo-effective CME/ICME characteristics. *J. Space Weather Space Clim.* 14, 6. doi:10.1051/swsc/2024004
- Napoletano, G., Forte, R., Del Moro, D., Pietropaolo, E., Giovannelli, L., and Berrilli, F. (2018). A probabilistic approach to the drag-based model. *J. Space Weather Space Clim.* 8, A11. doi:10.1051/swsc/2018003
- Napoletano, G., Foldes, R., Camporeale, E., de Gasperis, G., Giovannelli, L., Paouris, E., et al. (2022). Parameter distributions for the drag-based modeling of CME propagation. *Space weather.* 20, e2021SW002925. doi:10.1029/2021SW
- Odstrcil, D., Pizzo, V. J., Linker, J. A., Riley, P., Lionello, R., and Mikic, Z. (2004). Initial coupling of coronal and heliospheric numerical magnetohydrodynamic codes. *J. Atmos. Sol. Terr. Phys.* 66, 1311–1320. doi:10.1016/j.jastp.2004.
- Riley, P., Linker, J. A., and Mikić, Z. (2013). On the application of ensemble modeling techniques to improve ambient solar wind models. *J. Geophys. Res.* 118, 600–607. doi:10.1002/jgra.50156
- Rollett, T., Möstl, C., Isavnin, A., Davies, J. A., Kubicka, M., Amerstorfer, U. V., et al. (2016). ELEvoHI: a novel CME prediction tool for heliospheric imaging combining an elliptical front with drag-based model fitting. *Astrophys. J.* 824, 131. doi:10.3847/0004-637X/824/2/131

Rossi, M., Guastavino, S., Piana, M., and Massone, A. M. (2025). Extended drag-based model for better predicting the evolution of coronal mass ejections. *Astron. Astrophys.* 694, A247. doi:10.1051/0004-6361/202452288

- Schwenn, R., Dal Lago, A., Huttunen, E., and Gonzalez, W. D. (2005). The association of coronal mass ejections with their effects near the Earth. *Ann. Geophys.* 23, 1033–1059. doi:10.5194/angeo-23-1033-2005
- Shanmugaraju, A., and Vršnak, B. (2014). Transit time of coronal mass ejections under different ambient solar wind conditions. *Sol. Phys.* 289, 339–349. doi:10.1007/s11207-013-0322-8
- Shi, T., Wang, Y., Wan, L., Cheng, X., Ding, M., and Zhang, J. (2015). Predicting the arrival time of coronal mass ejections with the graduated cylindrical shell and drag force model.  $Astrophys.\ J.\ 806, 271.\ doi:10.1088/0004-637X/806/2/271$
- Siscoe, G., and Schwenn, R. (2006). CME disturbance forecasting. *Space Sci. Rev.* 123, 453–470. doi:10.1007/s11214-006-9024-v
- Smith, Z., and Dryer, M. (1990). MHD study of temporal and spatial evolution of simulated interplanetary shocks in the ecliptic plane within 1 AU. *Sol. Phys.* 129, 387–405. doi:10.1007/BF00159049
- Stamkos, S., Patsourakos, S., Vourlidas, A., and Daglis, I. A. (2023). How magnetic erosion affects the drag-based kinematics of fast coronal mass ejections. *Sol. Phys.* 298, 88. doi:10.1007/s11207-023-02178-7
- Sudar, D., Vršnak, B., and Dumbović, M. (2016). Predicting coronal mass ejections transit times to Earth with neural network. *Mon. Not. R. Astron. Soc.* 456, 1542–1548. doi:10.1093/mnras/stv2782
- Sudar, D., Vršnak, B., Dumbović, M., Temmer, M., and Čalogović, J. (2022). Influence of the drag force on the leading edge of a coronal mass ejection. *Astron. Astrophys.* 665, A142. doi:10.1051/0004-6361/202244114
- Tóth, G., Van der Holst, B., Sokolov, I. V., De Zeeuw, D. L., Gombosi, T. I., Fang, F., et al. (2012). Adaptive numerical algorithms in space weather modeling. *J. Comput. Phys.* 231, 870–903. doi:10.1016/j.jcp.2011.02.006
- Vakhrusheva, A. A., Kaportseva, K. B., Shugay, Yu.S., Eremeev, V. E., and Kalegaev, V. V. (2024). Modeling arrival time of coronal mass ejections to near-Earth orbit using coronal dimming parameters. *Cosm. Res.* 62, 350–358. doi:10.1134/S0010952524600422
- Vourlidas, A., Patsourakos, S., and Savani, N. P. (2019). Predicting the geoeffective properties of coronal mass ejections: current status, open issues and path forward. *Phil. Trans. R. Soc. A* 377, 20180096. doi:10.1098/rsta.2018.0096
- Vršnak, B. (2021). Analytical and empirical modelling of the origin and heliospheric propagation of coronal mass ejections, and space weather applications. *J. Space Weather Space Clim.* 11, 34. doi:10.1051/swsc/2021012
- Vršnak, B., and Gopalswamy, N. (2002). Influence of the aerodynamic drag on the motion of interplanetary ejecta. *J. Geophys. Res.* 107 (SSH 2-1), 2–6. doi:10.1029/2001JA000120
- Vršnak, B., and Žic, T. (2007). Transit times of interplanetary coronal mass ejections and the solar wind speed. *Astron. Astrophys.* 472, 937–943. doi:10.1051/0004-6361:20077499
- Vršnak, B., Žic, T., Vrbanec, D., Temmer, M., Rollett, T., Möstl, C., et al. (2013). Propagation of interplanetary coronal mass ejections: the drag-based model. *Sol. Phys.* 285, 295–315. doi:10.1007/s11207-012-0035-4
- Wang, Y. M., Shen, C. L., Wang, S., and Ye, P. Z. (2004). Deflection of coronal mass ejection in the interplanetary medium. Sol. Phys. 222, 329–343. doi:10.1023/B:SOLA.0000043576.21942.aa
- Wang, Y. M., Zhou, Z. J., Liu, J. J., Shen, C. L., and Wang, S. (2013). Dynamic process of coronal mass ejections in interplanetary space (in Chinese). *Sci. Sin. Terrae* 43, 934–950. doi:10.1360/zd-2013-43-6-934
- Wang, J. J., Ao, X. Z., Wang, Y. M., Wang, C. B., Cai, Y. X., Luo, B. X., et al. (2018). An operational solar wind prediction system transitioning fundamental science to operations. *J. Space Weather Space Clim.* 8, A39. doi:10.1051/swsc/2018025
- Wu, C. C., Dryer, M., Wu, S. T., Wood, B. E., Fry, C. D., Liou, K., et al. (2011). Global three-dimensional simulation of the interplanetary evolution of the observed geoeffective coronal mass ejection during the epoch 1–4 August 2010. *J. Geophys. Res.* 116, A12103. doi:10.1029/2011JA016947
- Yordanova, E., Temmer, M., Dumbović, M., Scolini, C., Paouris, E., Werner, A. L. E., et al. (2024). Refined modeling of geoeffective fast halo CMEs during solar cycle 24. *Space weather.* 22, e2023SW003497. doi:10.1029/2023SW003497
- Zhao, X. H., and Dryer, M. (2014). Current status of CME/shock arrival time prediction. Space weather. 12, 448–469. doi:10.1002/2014SW001060
- Zhao, X. H., and Feng, X. S. (2014). Shock propagation model version 2 and its application in predicting the arrivals at Earth of interplanetary shocks during solar cycle 23. *J. Geophys. Res.* 119, 1–10. doi:10.1002/2012JA018503
- Zhuang, B., Wang, Y. M., Hu, Y. Q., Shen, C. L., Liu, R., Gou, T. Y., et al. (2019). Numerical simulations on the deflection of coronal mass ejections in the interplanetary space. *Astrophys. J.* 876, 73. doi:10.3847/1538-4357/ab139e
- Žic, T., Vršnak, B., and Temmer, M. (2015). Heliospheric propagation of coronal mass ejections: drag-based model fitting. *Astrophys. J. Suppl. Ser.* 218, 32. doi:10.1088/0067-0049/218/2/32